Gravitational wave imprints of the doublet left-right symmetric model

Siddhartha Karmakar[1,2,*] and Dhruv Ringe[3,†]

[1]*Department of Mathematics, Indian Institute of Technology
Bombay, Powai, Mumbai, Maharashtra-400076, India*
[2]*Department of Theoretical Physics, Tata Institute of Fundamental Research,
Colaba, Mumbai, Maharashtra-400005, India*
[3]*Department of Physics, Indian Institute of Technology
Indore, Khandwa Road, Simrol, Indore, Madhya Pradesh-453552, India*

We study the stochastic gravitational wave (GW) background resulting from the strong first-order phase transition (SFOPT) associated with $SU(2)_R \times U(1)_{B-L}$-breaking in the doublet left-right symmetric model (DLRSM). For different values of the symmetry-breaking scale $v_R = 20$, 30, and 50 TeV, we construct the one-loop finite temperature effective potential to explore the parameter space for regions showing SFOPT. We identify the region where the associated GW background is strong enough to be detected at planned GW observatories. A strong GW signature favors a relatively light CP-even neutral scalar H_3, arising from the $SU(2)_R$ doublet. The $SU(2)_L$ subgroup of DLRSM is broken by three vacuum expectation values: κ_1, κ_2, and v_L. We observe a preference for $\mathcal{O}(1)$ values of the ratio $w = v_L/\kappa_1$, but no clear preference for the ratio $r = \kappa_2/\kappa_1$. A large number of points with strong GW signal can be ruled out from precise measurement of the trilinear Higgs coupling and searches for H_3 at the future colliders.

I. INTRODUCTION

Left-right symmetric models (LRSMs) [1–5] provide an attractive scenario for addressing several limitations of the standard model (SM). In LRSM, the SM gauge group is extended from $\mathcal{G}_{SM} = SU(3)_c \times SU(2)_L \times U(1)_Y$ to $\mathcal{G}_{LRSM} = SU(3)_c \times SU(2)_L \times SU(2)_R \times U(1)_{B-L}$, and the right-chiral fermions transform as doublets under the $SU(2)_R$ subgroup. The nonobservation of a right-handed charged current at colliders puts a lower bound on the $SU(2)_R \times U(1)_{B-L}$-breaking scale, $v_R \gtrsim \mathcal{O}(10)$ TeV, while the upper bound remains unconstrained.

There are different realizations of LRSM, depending on the scalars involved in the spontaneous breaking of $\mathcal{G}_{LRSM}$ to $\mathcal{G}_{SM}$. These also differ in the mechanism for generating fermion masses. The triplet left-right symmetric model (TLRSM) [6–8], contains a scalar bidoublet, and two $SU(2)$ triplets. The charged fermion masses are then generated by the bidoublet, whereas the neutrino masses are generated by the type-II seesaw mechanism [9]. On the

other hand, the scalar sector of a doublet left-right symmetric model (DLRSM) consists of a scalar bidoublet and a pair of $SU(2)$ doublets [5,10]. In DLRSM, neutrino masses can be incorporated by extending the model with an additional charged singlet scalar [11–14]. Contrary to TLRSM, where the vacuum expectation value (*vev*) of the triplets is constrained to be small, there are no sources of custodial symmetry breaking in DLRSM at the tree level. Apart from TLRSM and DLRSM, other variations have also been discussed in the literature and have different experimental consequences [15–18].

The era of gravitational wave (GW) astronomy was kickstarted by the observation of GW from a binary black hole merger by the aLIGO collaboration in 2015 [19]. Several ground-based and space-based observatories such as LISA [20], DECIGO [21], BBO [22], ET [23], and CE [24] are planned and will be functional in the coming decades. Various phenomena in the early universe, such as inflation, cosmic strings, domain walls, and strong first-order phase transitions (SFOPT) can lead to a stochastic GW background [25–28]. The upcoming GW observatories will be capable of detecting the GW background from SFOPT up to symmetry-breaking scales as high as 10^6–10^7 GeV [29–31].

In the context of LRSM, GW astronomy presents a novel approach to probe the scale v_R by studying the possibility of an observable GW background from SFOPT within the

---

*karmakars@iitb.ac.in
†phd1901151004@iiti.ac.in

LRSM. Different realizations of LRSM have been explored in the literature for GW imprints: through SFOPT in TRLSM [32,33], and in an LR model with seesawlike fermion mass generation [17], and also from domain walls arising out of the breaking of the discrete parity symmetry [34]. However, GW imprints of DLRSM have not yet been explored in the literature. Recently it was shown that the pattern of electroweak symmetry breaking (EWSB) in DLRSM can be vastly different from the other versions of LRSM, with interesting consequences from precision observables [35] and Higgs data [36]. It is therefore interesting to study the GW signature in DLRSM.

EWSB in DLRSM happens via three *vev*s: κ_1, κ_2, coming from the bidoublet, and v_L coming from the $SU(2)_L$ doublet. These are constrained by the relation, $\kappa_1^2 + \kappa_2^2 + v_L^2 = v^2$, where $v = 246$ GeV. It is useful to define the *vev* ratios: $r = \kappa_2/\kappa_1$, $w = v_L/\kappa_1$. As the custodial symmetry is preserved at the tree level, the *vev*s κ_1, κ_2, and v_L can all be sizable, i.e. r and w can be $\mathcal{O}(0.1)$ and $\mathcal{O}(1)$ respectively. In Ref. [35], it was shown that the EW precision data prefers a large value of w. Further, in Ref. [36] it was shown that the measurement of the Higgs signal strength and meson mixing bounds prefer large values of r and w. It is therefore interesting to note that, unlike TLRSM, EWSB in DLRSM can be considerably different from that in SM, even though the $SU(2)_R \times U(1)_{B-L}$-breaking dynamics is decoupled from the EW scale. In this paper, we ask (i) whether DLRSM can lead to a detectable GW background in some region of the parameter space, and (ii) whether this region of the parameter space prefers a special pattern of EWSB.

The rest of the paper is organized as follows. In Sec. II, we give a brief review of DLRSM: field content, symmetry breaking, and mass generation in the gauge, fermion, and gauge sectors. In Sec. II D and Sec. II E, we discuss the theoretical bounds and the constraints from the Higgs data respectively. In Sec. III, we construct the one-loop finite temperature effective potential required to study the phase transition (PT) associated with $SU(2)_R \times U(1)_{B-L}$-breaking. We then describe our procedure for scanning the parameter space in Sec. IV. In Sec. V, we discuss the GW background obtained for points with SFOPT. In Sec. VI, we compute the signal-to-noise ratio (SNR) for six benchmark points, at various planned GW detectors such as FP-DECIGO, BBO, and Ultimate-DECIGO. In Sec. VII, we discuss future collider probes that can complement the GW signal. Finally, in Sec. VIII, we summarize our key findings and present concluding remarks.

II. THE MODEL

We follow the notation of Refs. [35,36] for the scalar potential and *vev* structure of the scalar multiplets. The fermion content of the model has the following charges under the LRSM gauge group, $\mathcal{G}_{\text{LRSM}} = SU(3)_c \times SU(2)_L \times SU(2)_R \times U(1)_{B-L}$,

$$Q_L = \begin{pmatrix} u_L \\ d_L \end{pmatrix} \sim (3, 2, 1, 1/3),$$

$$Q_R = \begin{pmatrix} u_R \\ d_R \end{pmatrix} \sim (3, 1, 2, 1/3),$$

$$L_L = \begin{pmatrix} \nu_L \\ e_L \end{pmatrix} \sim (1, 2, 1, -1),$$

$$L_R = \begin{pmatrix} \nu_R \\ e_R \end{pmatrix} \sim (1, 1, 2, -1), \qquad (2.1)$$

where the quantum numbers of the multiplets under the subgroups of $\mathcal{G}_{\text{LRSM}}$ are indicated in brackets. We have suppressed the family index $i \in \{1, 2, 3\}$ for three generations of quarks and three generations of leptons. The right-handed neutrino ν_R is needed to complete the $SU(2)_R$ lepton doublet. This choice of fermions is required for the cancellation of the $U(1)_{B-L}$ gauge anomaly and ensures that the model is manifestly symmetric under the transformations: $Q_L \leftrightarrow Q_R$, $L_L \leftrightarrow L_R$.

A. Scalar sector

The scalar sector of DLRSM includes a complex bidoublet Φ needed to generate charged fermion masses, and two doublets χ_L and χ_R, which participate in the EW- and LR-symmetry breaking respectively. These scalar multiplets and their charges under $\mathcal{G}_{\text{LRSM}}$ are:

$$\Phi = \begin{pmatrix} \phi_1^0 & \phi_2^+ \\ \phi_1^- & \phi_2^0 \end{pmatrix} \sim (1, 2, 2, 0),$$

$$\chi_L = \begin{pmatrix} \chi_L^+ \\ \chi_L^0 \end{pmatrix} \sim (1, 2, 1, 1),$$

$$\text{and} \quad \chi_R = \begin{pmatrix} \chi_R^+ \\ \chi_R^0 \end{pmatrix} \sim (1, 1, 2, 1). \qquad (2.2)$$

We take the potential to be parity-symmetric, i.e., the couplings of "L" and "R" fields are equal. This imposes an additional discrete symmetry $\mathcal{P}: L \leftrightarrow R$ on the Lagrangian. The most general, *CP*-conserving, renormalizable scalar potential is then given by,

$$V = V_2 + V_3 + V_4,$$

$$V_2 = -\mu_1^2 \mathrm{Tr}(\Phi^\dagger \Phi) - \mu_2^2 [\mathrm{Tr}(\tilde{\Phi}\Phi^\dagger) + \mathrm{Tr}(\tilde{\Phi}^\dagger \Phi)] - \mu_3^2 [\chi_L^\dagger \chi_L + \chi_R^\dagger \chi_R],$$

$$V_3 = \mu_4 [\chi_L^\dagger \Phi \chi_R + \chi_R^\dagger \Phi^\dagger \chi_L] + \mu_5 [\chi_L^\dagger \tilde{\Phi} \chi_R + \chi_R^\dagger \tilde{\Phi}^\dagger \chi_L],$$

$$V_4 = \lambda_1 [\mathrm{Tr}(\Phi^\dagger \Phi)]^2 + \lambda_2 [[\mathrm{Tr}(\tilde{\Phi}\Phi^\dagger)]^2 + [\mathrm{Tr}(\tilde{\Phi}^\dagger \Phi)]^2] + \lambda_3 \mathrm{Tr}(\tilde{\Phi}\Phi^\dagger)\mathrm{Tr}(\tilde{\Phi}^\dagger \Phi)$$

$$+ \lambda_4 \mathrm{Tr}(\Phi^\dagger \Phi)[\mathrm{Tr}(\tilde{\Phi}\Phi^\dagger) + \mathrm{Tr}(\tilde{\Phi}^\dagger \Phi)] + \rho_1 [(\chi_L^\dagger \chi_L)^2 + (\chi_R^\dagger \chi_R)^2] + \rho_2 \chi_L^\dagger \chi_L \chi_R^\dagger \chi_R$$

$$+ \alpha_1 \mathrm{Tr}(\Phi^\dagger \Phi)[\chi_L^\dagger \chi_L + \chi_R^\dagger \chi_R] + \left\{ \frac{\alpha_2}{2} [\chi_L^\dagger \chi_L \mathrm{Tr}(\tilde{\Phi}\Phi^\dagger) + \chi_R^\dagger \chi_R \mathrm{Tr}(\tilde{\Phi}^\dagger \Phi)] + \mathrm{H.c.} \right\}$$

$$+ \alpha_3 [\chi_L^\dagger \Phi \Phi^\dagger \chi_L + \chi_R^\dagger \Phi^\dagger \Phi \chi_R] + \alpha_4 [\chi_L^\dagger \tilde{\Phi}\tilde{\Phi}^\dagger \chi_L + \chi_R^\dagger \tilde{\Phi}^\dagger \tilde{\Phi} \chi_R], \tag{2.3}$$

with $\tilde{\Phi} \equiv \sigma_2 \Phi^* \sigma_2$. The potential has mass parameters: $\{\mu_{1,2,3,4,5}\}$, and quartic couplings: $\{\lambda_{1,2,3,4}, \alpha_{1,2,3,4}, \rho_{1,2}\}$. We assume all parameters to be real for simplicity.

The neutral scalars can be written in terms of real and imaginary components,

$$\phi_1^0 = \frac{1}{\sqrt{2}}(\phi_{1r}^0 + i\phi_{1i}^0), \qquad \phi_2^0 = \frac{1}{\sqrt{2}}(\phi_{2r}^0 + i\phi_{2i}^0),$$

$$\chi_L^0 = \frac{1}{\sqrt{2}}(\chi_{Lr}^0 + i\chi_{Li}^0), \qquad \chi_R^0 = \frac{1}{\sqrt{2}}(\chi_{Rr}^0 + i\chi_{Ri}^0). \tag{2.4}$$

We assign nonzero *vev*s only to the real components of the neutral scalars and do not consider *CP*- or charge-breaking minima. The *vev* structure is denoted by

$$\langle \Phi \rangle = \frac{1}{\sqrt{2}}\begin{pmatrix} \kappa_1 & 0 \\ 0 & \kappa_2 \end{pmatrix}, \qquad \langle \chi_L \rangle = \frac{1}{\sqrt{2}}\begin{pmatrix} 0 \\ v_L \end{pmatrix},$$

$$\langle \chi_R \rangle = \frac{1}{\sqrt{2}}\begin{pmatrix} 0 \\ v_R \end{pmatrix}. \tag{2.5}$$

The pattern of symmetry breaking is as follows:

$$SU(2)_L \times SU(2)_R \times U(1)_{B-L} \xrightarrow{v_R} SU(2)_L$$
$$\times U(1)_Y \xrightarrow{\kappa_1, \kappa_2, v_L} U(1)_Y.$$

The *vev* v_R of the doublet χ_R breaks $SU(2)_R \times U(1)_{B-L}$, while the three *vev*s κ_1, κ_2, and v_L trigger EWSB. Note that the discrete LR symmetry $\mathcal{P}$, is also broken by v_R, which leads to the formation of domain walls [34,37–41]. Such a domain wall network can dominate the energy density of the universe at late times. To avoid domination, a small bias term can be introduced via explicit LR-breaking operators, so that the domain walls become unstable and decay before the epoch of big bang nucleosynthesis. For example, the bias was generated by Planck-suppressed higher dimensional operators in Ref. [34]. Due to large suppression, these do not affect the nature and strength of the $SU(2)_R \times U(1)_{B-L}$ breaking PT.

As mentioned earlier, the EW *vev*s can be conveniently expressed in terms of the *vev* ratios r and w as, $\kappa_2 = r\kappa_1$ and $v_L = w\kappa_1$. Then, $\kappa_1^2(1 + r^2 + w^2) = v^2$, i.e., the value of κ_1 is fixed for a given r and w. The absence of a right-handed charged current in collider experiments implies a hierarchy of scales $v_R \gg v$.

In terms of the *vev*s κ_1, κ_2, v_L, and v_R, the minimization conditions are,

$$\frac{\partial V}{\partial \kappa_1} = \frac{\partial V}{\partial \kappa_2} = \frac{\partial V}{\partial v_L} = \frac{\partial V}{\partial v_R} = 0. \tag{2.6}$$

Using the minimization conditions, we trade $\mu_1^2, \mu_2^2, \mu_3^2$, and μ_5 for the *vev*s, μ_4, and quartic couplings (see Appendix A for full expressions). Thus the parameters of the DLRSM scalar sector reduce to

$$\{\lambda_{1,2,3,4}, \alpha_{1,2,3,4}, \rho_{1,2}, \mu_4, r, w, v_R\}. \tag{2.7}$$

The *CP*-even, *CP*-odd, and charged scalar mass matrices are obtained using

$$m_{ij}^2 = \left.\frac{\partial^2 V}{\partial \varphi_i \partial \varphi_j}\right|_{\langle \varphi \rangle}, \tag{2.8}$$

where

$$\varphi \equiv \{\phi_{1r}^0, \phi_{2r}^0, \chi_{Lr}^0, \chi_{Rr}^0, \phi_{1i}^0, \phi_{2i}^0, \chi_{Li}^0, \chi_{Ri}^0, \phi_1^\pm, \phi_2^\pm, \chi_L^\pm, \chi_R^\pm\}. \tag{2.9}$$

Physical scalar masses and mixing angles are obtained by diagonalizing these matrices. We denote the physical spectrum of scalars by: *CP*-even scalars, h, H_1, H_2, H_3, *CP*-odd scalars, A_1, A_2, and the charged scalars, $H_1^\pm, H_2^\pm$.

The lightest *CP*-even scalar, h has a mass of the order v, and is identified with the SM-like Higgs with mass ~ 125 GeV. Using nondegenerate perturbation theory, m_h is estimated as [35,36]

$$m_{h,\text{analytic}}^2 = \frac{\kappa_1^2}{2(1+r^2+w^2)}(4(\lambda_1(r^2+1)^2+4r(\lambda_4(r^2+1)+r\lambda_{23})+w^2(\alpha_{124}+r^2(\alpha_1+\alpha_3)+\alpha_2 r)$$

$$+ \rho_1 w^4) - \frac{1}{\rho_1}(\alpha_{124}+r^2(\alpha_1+\alpha_3)+\alpha_2 r+2\rho_1 w^2)^2), \tag{2.10}$$

where, $\alpha_{124} \equiv \alpha_1 + r\alpha_2 + \alpha_4$, and $\lambda_{23} = 2\lambda_2 + \lambda_3$. In the limit $r, w \to 0$, the above expression simplifies to

$$m_{h,\text{analytic}}^2 = v^2 \left(2\lambda_1 - \frac{(\alpha_1+\alpha_4)^2}{2\rho_1}\right). \tag{2.11}$$

However, it was pointed out in Ref. [36] that for certain values of the quartic parameters, the analytical estimate for m_h may not suffice.

The other scalars have masses of the order v_R. To $\mathcal{O}(\kappa_1/v_R)$, these masses are related to each other as

$$m_{H_1}^2 \simeq m_{A_1}^2 \simeq m_{H_1^\pm}^2 \approx \frac{1}{2}(\alpha_3 - \alpha_4)v_R^2,$$

$$m_{H_2}^2 \simeq m_{A_2}^2 \simeq m_{H_2^\pm}^2 \approx \frac{1}{2}(\rho_2 - 2\rho_1)v_R^2,$$

$$m_{H_3}^2 = 2\rho_1 v_R^2,$$

$$m_{H_2}^2 > m_{H_1}^2.$$

The first two mass expressions are valid in the limit $r, w \to 0$. Positive-definite nature of the CP-even mass

matrix leads to two approximate criteria: $\rho_2 > 2\rho_1$ and $\alpha_3 > \alpha_4$. In our analysis, we calculate the scalar masses and mixing numerically. The full analytic expressions at the leading order can be found in the Appendix of Ref. [36].

For the CP-even scalars, the mass-squared matrix is diagonalized by the orthogonal matrix O,

$$O^T \mathcal{M}_{\text{CPE}}^2 O = (\mathcal{M}_{\text{CPE}}^{\text{diag}})^2, \qquad X_{\text{physical}} = O^T X, \tag{2.12}$$

where $X = (\phi_{1r}^0, \phi_{2r}^0, \chi_{Lr}^0, \chi_{Rr}^0)^T$, $X_{\text{physical}} = (h, H_1, H_2, H_3)^T$. The scalars H_1 and A_1 can contribute to the mixing of $K_0 - \bar{K}_0$ system, leading to the constraint, $m_{H_1, A_1} > 15$ TeV [42]. The scalar H_3 predominantly originates from the doublet χ_R and its coupling to the SM particles is suppressed by the element $O_{41} \sim v^2/v_R^2$. So, collider searches allow it to be much lighter than H_1.

The triple Higgs coupling (c_{h^3}) in DLRSM is given by [36]

$$c_{h^3} = \frac{\kappa_1}{2}(2(\lambda_1 + r\lambda_4)O_{11}^3 + 2(r\lambda_1 + \lambda_4)O_{21}^3 + 2w\rho_1 O_{31}^3 + 2(r(\lambda_1 + 4\lambda_2 + 2\lambda_3) + 3\lambda_4)O_{11}^2 O_{21}$$

$$+ 2(\lambda_1 + 4\lambda_2 + 2\lambda_3 + 3\lambda_4 r)O_{11}O_{21}^2 + w(\alpha_1 + \alpha_4)O_{11}^2 O_{31} + (\alpha_1 + r\alpha_2 + \alpha_4)O_{11}O_{31}^2$$

$$+ w(\alpha_1 + \alpha_3)O_{21}^2 O_{31} + (\alpha_2 + r(\alpha_1 + \alpha_3))O_{21}O_{31}^2), \tag{2.13}$$

with the corresponding coupling multiplier $\kappa_h = c_{h^3}/c_{h^3}^{\text{SM}}$, where $c_{h^3}^{\text{SM}} = m_h^2/2v = \lambda^{\text{SM}}v$.

B. Fermion sector

The fermion multiplets couple to the bidoublet Φ via Yukawa terms:

$$\mathcal{L}_Y \supset -\bar{Q}_{Li}(y_{ij}\Phi + \tilde{y}_{ij}\tilde{\Phi})Q_{Rj} + \text{H.c.}, \tag{2.14}$$

which leads to the mass matrices for the quarks:

$$M_U = \frac{1}{\sqrt{2}}(\kappa_1 y + \kappa_2 \tilde{y}), \qquad M_D = \frac{1}{\sqrt{2}}(\kappa_2 y + \kappa_1 \tilde{y}),$$

where M_U and M_D stand for up-type and down-type mass matrices in the flavor basis respectively. To obtain the

physical basis of fermions, these mass matrices need to be diagonalized through unitary transformations described by the left- and right-handed CKM matrices ($V_{L,R}^{\text{CKM}}$). Manifest left-right symmetry implies $V_R^{\text{CKM}} = V_L^{\text{CKM}}$. For the calculation of the effective potential in the next section, it is enough to take $y \approx \text{diag}(0, 0, y_{33})$ and $\tilde{y} \approx \text{diag}(0, 0, \tilde{y}_{33})$. In the limit $V_{33}^{\text{CKM}} \approx 1$,

$$y_{33} = \frac{\sqrt{2}(1+r^2+w^2)^{1/2}}{v(1-r^2)}(m_t - rm_b),$$

$$\tilde{y}_{33} = \frac{\sqrt{2}(1+r^2+w^2)^{1/2}}{v(1-r^2)}(m_b - rm_t), \tag{2.15}$$

where the top and bottom quark masses are $m_t = 173.5$ GeV, and $m_b \approx 5$ GeV. In the limit $r, w \to 0$, y_{33} and $\tilde{y}_{33}$ reduce to the SM Yukawa couplings y_t and y_b

respectively. However, we do not make any such assumption and use Eq. (2.15), allowing r, w to be arbitrary.

The couplings of the SM-like Higgs with the third-generation quarks are given by:

$$c_{htt(hbb)} = \frac{\kappa_1}{\kappa_-^2}((O_{11} - rO_{21})m_{t(b)}$$
$$+ (O_{21} - rO_{11})(V_L^{CKM}\hat{M}_{D(U)}V_R^{CKM\dagger})_{33}), \quad (2.16)$$

where $\kappa_-^2 = \kappa_1^2 - \kappa_2^2 = \kappa_1^2(1 - r^2)$ and $\hat{M}_{U(D)}$ denotes the diagonal up (down)-type quark mass matrix. Here O_{ij} are the elements of the orthogonal transformation matrix appearing in Eq. (2.12). Then the coupling multipliers, κ_b and κ_t are: $\kappa_f = c_{hff}/c_{hff}^{SM}$, where $c_{hff}^{SM} = m_f/v$ and $f = t, b$.

Since $V_{L,R}^{CKM} \approx \mathbf{1}$, Eq. (2.16), becomes,

$$c_{htt} \approx \frac{\kappa_1}{\kappa_-^2}(O_{11}(m_t - rm_b) + O_{21}(m_b - rm_t)),$$
$$c_{hbb} \approx \frac{\kappa_1}{\kappa_-^2}(O_{11}(m_b - rm_t) + O_{21}(m_t - rm_b))$$

Note that there is a hierarchy, $O_{21} \ll O_{11} \sim 1$, $m_t \gg m_b$, and $r \ll 1$. The SM couplings are recovered by setting $O_{11} = 1$, $O_{21} = 0$, $r = 0$, in the above expressions. For a large $\phi_{1r}^0 - \phi_{2r}^0$ mixing, i.e., $O_{21} \gtrsim \mathcal{O}(10^{-2})$ or large κ_2, i.e., $r \sim \mathcal{O}(10^{-1})$, the deviation of $hb\bar{b}$ coupling from the SM value can be quite large due to the multiplicative factors proportional to $O_{21}m_t$, and $rO_{11}m_t$. On the other hand, the deviation of $ht\bar{t}$ coupling is proportional to $O_{21}m_b$ and $rO_{21}m_t$, and is therefore rather small for the current precision of κ_t measurement.

The Yukawa term for leptons is similar to that of quarks given in Eq. (2.14). However, since neutrino masses are tiny, generating them in DLRSM would lead to a large hierarchy among lepton Yukawa couplings. Moreover, the neutrinos could be Majorana, in which case DLRSM cannot account for them. In Refs. [11–14], neutrino masses were explained by adding a singlet charged scalar to DLRSM. In Appendix C, we show that this extra field does not modify the strength of FOPT.

C. Gauge sector

In this paper, we work under the assumption of manifest left-right symmetry of the UV-Lagrangian, i.e., $g_R = g_L = g$. Here, $g_{L(R)}$ are the gauge couplings of $SU(2)_{L(R)}$, and g is the $SU(2)_L$ gauge coupling of SM. The mass matrix for charged gauge bosons is

$$\mathcal{L}_{mass} \supset \frac{g^2}{8}(W_L^+ \quad W_R^+)\begin{pmatrix} v^2 & -2\kappa_1\kappa_2 \\ -2\kappa_1\kappa_2 & V^2 \end{pmatrix}\begin{pmatrix} W_L^- \\ W_R^- \end{pmatrix}, \quad (2.17)$$

where, $v^2 = \kappa_1^2 + \kappa_2^2 + v_L^2$ and $V^2 = \kappa_1^2 + \kappa_2^2 + v_R^2$. The physical charged gauge bosons have masses,

$$m_{W_{1,2}}^2 = \frac{g^2}{4}(v^2 + V^2 \mp \sqrt{(v^2 - V^2)^2 + 16\kappa_1^2\kappa_2^2}), \quad (2.18)$$

$W_1^\pm$ is identified as the SM $W^\pm$ boson and $W_2^\pm$ is the new charged gauge boson with mass $\sim\mathcal{O}(v_R)$. The mixing matrix is characterized by an orthogonal rotation with angle $\xi \simeq 2\kappa_1\kappa_2/v_R^2$.

Similarly, the neutral gauge boson mass matrix is,

$$\mathcal{L}_{mass} \supset \frac{1}{8}(W_L^{3\mu} \quad W_R^{3\mu} \quad B^\mu)\begin{pmatrix} g^2v^2 & -g^2\kappa_+^2 & -gg_{BL}v_L^2 \\ & g^2V^2 & -gg_{BL}v_R^2 \\ & & g_{BL}^2(v_L^2 + v_R^2) \end{pmatrix}\begin{pmatrix} W_{L\mu}^3 \\ W_{R\mu}^3 \\ B_\mu \end{pmatrix}, \quad (2.19)$$

where $\kappa_+^2 = \kappa_1^2 + \kappa_2^2$, g_{BL} is the gauge coupling of $U(1)_{B-L}$ and here some of the elements have been suppressed since the matrix is symmetric. The lightest eigenstate is massless and identified as the photon, while the other two states have masses

$$m_{Z_1,Z_2}^2 = \frac{1}{8}(g^2v^2 + g^2V^2 + g_{BL}^2(v_L^2 + v_R^2)$$
$$\mp \sqrt{(g^2v^2 + g^2V^2 + g_{BL}^2(v_L^2 + v_R^2))^2 + 4(g^4 + 2g^2g_{BL}^2)(\kappa_+^4 - v^2V^2)}). \quad (2.20)$$

The lighter mass eigenstate Z_1 corresponds to the SM Z boson, while Z_2 has a mass $\sim\mathcal{O}(v_R)$.

In the limit $\kappa_1, \kappa_2, v_L \ll v_R$ the mixing matrix is [43]

$$
\begin{pmatrix} A_\mu \\ Z_{1\mu} \\ Z_{2\mu} \end{pmatrix} = \begin{pmatrix} s_W & c_W s_Y & c_W c_Y \\ -c_W & s_W s_Y & s_W c_Y \\ 0 & c_Y & s_Y \end{pmatrix} \begin{pmatrix} W^3_{L\mu} \\ W^3_{R\mu} \\ B_\mu \end{pmatrix}, \qquad (2.21)
$$

where

$$
s_W \equiv \sin\theta_W = \frac{g_{BL}}{\sqrt{g^2 + 2g_{BL}^2}}, \quad c_W \equiv \cos\theta_W = \sqrt{\frac{g^2 + g_{BL}^2}{g^2 + 2g_{BL}^2}},
$$

$$
s_Y \equiv \sin\theta_Y = \frac{g_{BL}}{\sqrt{g^2 + g_{BL}^2}}, \quad c_Y \equiv \cos\theta_Y = \frac{g}{\sqrt{g^2 + g_{BL}^2}}.
$$
$$(2.22)$$

We fix $g_{BL} = gg'/(g^2 - g'^2)^{1/2}$, where g' is the gauge coupling for $U(1)_Y$ of SM. Direct searches for spin-1 resonances have put a lower limit on the masses of the new charged and neutral gauge bosons. In DLRSM, the masses of such new gauge bosons are $m_{W_2} \sim g v_R/2 =$ and $m_{Z_2} \sim m_{W_2}/\cos\theta_Y$. Recently, the lower limit on the mass of W_2 in DLRSM has been estimated to be, $m_{W_2} > 5.1$ TeV [44], which leads to a lower bound on v_R, $v_R > 2m_{W_2}/g = 15.7$ TeV. The constraint on m_{Z_2} is comparatively weaker, $m_{Z_2} > 4.3$ TeV. Therefore, the lowest value of v_R we use in our benchmark scenarios is $v_R = 20$ TeV.

D. Theoretical bounds

We incorporate the following theoretical constraints:
  (i) *Perturbativity:* The quartic couplings of the scalar potential, $\{\lambda_{1,2,3,4}, \alpha_{1,2,3,4}, \rho_{1,2}\}$, are subjected to the upper limit of 4π from perturbativity. Moreover, the Yukawa couplings of the DLRSM Lagrangian must satisfy the perturbativity bound $y_{33}, \tilde{y}_{33} < \sqrt{4\pi}$, with $y_{33}, \tilde{y}_{33}$ defined in Eq. (2.15), These constrain the value of *vev* ratios roughly to $r < 0.8$ and $w < 3.5$ [36].
  (ii) *Unitarity:* The scattering amplitudes of $2 \to 2$ processes involving scalars and gauge bosons must satisfy perturbative unitarity. To $\mathcal{O}(\kappa_1/v_R)$, these constraints can be expressed in terms of the masses of the new scalars in DLRSM [35],

$$
0 < \rho_1 < \frac{8\pi}{3}, \quad \text{or,} \quad \frac{m^2_{H_3}}{v_R^2} < \frac{16\pi}{3},
$$

$$
\frac{(c_{H_3})^2}{k^4} \frac{m^2_{H_3}}{v_R^2} < \frac{16\pi}{3},
$$

$$
2\frac{w^2}{k^2} \sum_{i=1,2} F_i^2 \frac{m^2_{H_i^\pm}}{v_R^2} + \frac{c_{H_3}}{k^2} \frac{m^2_{H_3}}{v_R^2} < 16\pi,
$$

$$
2\frac{w^2}{k^2} \sum_{i=1,2} S_i^2 \frac{m^2_{H_i^\pm}}{v_R^2} + \frac{c_{H_3}}{k^2} \frac{m^2_{H_3}}{v_R^2} < 16\pi, \qquad (2.23)
$$

where $k^2 = 1 + r^2 + w^2$ and F_i, S_i, and c_{H_3} are defined in terms of the parameters of the potential [35].
  (iii) *Boundedness from below:* The scalar potential must be bounded from below (BFB) along all directions in field space. This leads to additional constraints on the quartic couplings of the model. The full set of such constraints was derived in Ref. [36], which we have implemented in our numerical analysis.

E. Constraints from $h(125)$ data

In the following, we qualitatively describe the constraints on DLRSM from Higgs-related measurements at the LHC.
  (i) The key constraint comes from the measurement of the mass of SM-like Higgs, $m_h = 125.38 \pm 0.14$ GeV [45]. If the theoretical bounds of perturbativity and boundedness from below are taken into account together with $m_{h,\text{analytic}} \simeq 125$ GeV, it leads to an upper bound on the *vev* ratio, $w \lesssim 2.93 + 4.35r - 0.48r^2$.
  (ii) One of the most stringent constraints on the DLRSM parameter space comes from the measurement of $hb\bar{b}$ coupling, $\kappa_b = 0.98^{+0.14}_{-0.13}$ [46]. If the mixing between ϕ^0_{1r} and ϕ^0_{2r} takes large values, κ_b can deviate from unity, thereby ruling out a large region of parameter space allowed by theoretical bounds and the measurement of m_h. However, $ht\bar{t}$ coupling is not significantly modified and does not result in any new constraints.
  (iii) As discussed in Sec. II C, a large value of v_R ensures that the mixings between the SM-like and heavier gauge bosons are rather small, $\xi \sim \mathcal{O}(v^2/v_R^2)$. Therefore, the $hW_1 W_1$ and $hZ_1 Z_1$ couplings are quite close to their SM values and do not lead to any additional constraints on the DLRSM parameter space.
  (iv) The trilinear coupling of the SM-like Higgs given in Eq. (2.13), does not necessarily align with the SM value. As seen in Eq. (2.13), for nonzero mixings, particularly, $O_{21} \neq 0$, the parameters appearing in the paranthesis can individually take a wide range of values, leading to a potentially significant deviation of c_{h^3} from $c_{h^3}^{\text{SM}}$. In our analysis, we impose the ATLAS bound of $\kappa_h = [-2.3, 10.3]$ at 95% CL [47].

III. EFFECTIVE POTENTIAL

In this section, we construct the full one-loop finite temperature effective potential [48,49] required to study the nature of the PT associated with the breaking of $SU(2)_R \times U(1)_{B-L}$. Below we describe the procedure step by step.

The tree-level effective potential is obtained by setting all the fields to their respective background field value in the potential given in Eq. (2.3). The *CP*-even neutral

component of χ_R is responsible for breaking the $SU(2)_R \times U(1)_{B-L}$ gauge group, whose background value we denote by R. Since $v_R \gg v$, all other field values can be set to zero. Hence, in the notation of Eq. (2.9), the background fields are

$$\langle \varphi \rangle = \{0, 0, 0, R, 0, 0, 0, 0, 0, 0, 0, 0, 0\}.$$

The tree-level effective potential is then given by

$$V_0(R) = -\frac{\mu_3^2}{2} R^2 + \frac{\rho_1}{4} R^4. \tag{3.1}$$

At the one-loop level, the zero-temperature correction to the effective potential is given by the Coleman-Weinberg (CW) formula [50]. In the Landau gauge, with $\overline{\text{MS}}$ renormalization scheme, the CW potential is [48]

$$V_{\text{CW}}(R) = \frac{1}{64\pi^2} \sum_i (-1)^{f_i} n_i m_i^4(R) \left[\log\left(\frac{m_i^2(R)}{\mu^2}\right) - c_i\right], \tag{3.2}$$

where i runs over all species coupling to the $SU(2)_R \times U(1)_{B-L}$-breaking field χ_{Rr}^0. The field-dependent mass, $m_i(R)$ is the mass of the species i in the presence of the background field R. When there is mixing between the different species, the masses are extracted as the eigenvalues of the corresponding mass matrices. The expressions for the field-dependent masses can be found in Appendix B. In Appendix C we take the minimal mechanism of neutrino mass generation of Refs. [11,12] and show that the right-handed neutrino ν_R and the extra charged scalar do not contribute to the effective potential. Therefore the contributions only come from the CP-even scalars: $\{\phi_{1r}^0, \phi_{2r}^0, \chi_{Lr}^0, \chi_{Rr}^0\}$, CP-odd scalars: $\{\phi_{1i}^0, \phi_{2i}^0, \chi_{Li}^0, \chi_{Ri}^0\}$, charged scalars: $\{\phi_1^\pm, \phi_2^\pm, \chi_L^\pm, \chi_R^\pm\}$, and gauge bosons $W_{L,R}^\pm$, $Z_{L,R}$ and B. The factor f_i is 0 (1) for bosons (fermions), and the number of degrees of freedom n_i are,

$$n_{\phi_{1r}^0} = n_{\phi_{2r}^0} = n_{\chi_{Lr}^0} = n_{\chi_{Rr}^0} = 1,$$

$$n_{\phi_{1i}^0} = n_{\phi_{2i}^0} = n_{\chi_{Li}^0} = n_{\chi_{Ri}^0} = 1,$$

$$n_{\phi_1^\pm} = n_{\phi_2^\pm} = n_{\chi_L^\pm} = n_{\chi_R^\pm} = 2,$$

$$n_{W_{Lt}^\pm} = n_{W_{Rt}^\pm} = 4,$$

$$n_{W_{Ll}^\pm} = n_{W_{Rl}^\pm} = 2,$$

$$n_{Z_{Lt}} = n_{Z_{Rt}} = n_{B_t} = 2,$$

$$n_{Z_{Ll}} = n_{Z_{Rl}} = n_{B_l} = 1.$$

The subscripts t and l stand for transverse and longitudinal polarizations of the gauge bosons. The constant $c_i = 5/6$ for gauge bosons, and $3/2$ for all other fields. We set the

renormalization scale $\mu = v_R$ to ensure the validity of the CW formula by having $\mathcal{O}(1)$ logs.

We impose the "on-shell" renormalization condition so that the position of the minimum and the mass of the CP-even scalar χ_{Rr}^0 calculated from the one-loop potential coincides with the corresponding tree-level value. This is achieved by introducing a counterterm potential

$$V_{\text{c.t.}}(R) = -\frac{\delta\mu_3^2}{2} R^2 + \frac{\delta\rho_1}{4} R^4, \tag{3.3}$$

where the unknown coefficients $\delta\mu_3^2$ and $\delta\rho_1$ are fixed by demanding

$$\frac{\partial}{\partial R} \left(V_{\text{CW}} + V_{\text{c.t.}}\right)\bigg|_{R=v_R} = 0, \tag{3.4a}$$

$$\frac{\partial^2}{\partial R^2} \left(V_{\text{CW}} + V_{\text{c.t.}}\right)\bigg|_{R=v_R} = 0. \tag{3.4b}$$

This leads to

$$\delta\mu_3^2 = \frac{3}{2v_R} \frac{\partial V_{\text{CW}}}{\partial R}\bigg|_{R=v_R} - \frac{1}{2} \frac{\partial^2 V_{\text{CW}}}{\partial R^2}\bigg|_{R=v_R}, \tag{3.5a}$$

$$\delta\rho_1 = \frac{1}{2v_R^3} \frac{\partial V_{\text{CW}}}{\partial R}\bigg|_{R=v_R} - \frac{1}{2v_R^2} \frac{\partial^2 V_{\text{CW}}}{\partial R^2}\bigg|_{R=v_R}. \tag{3.5b}$$

Then the one-loop contribution to the effective potential is

$$V_1 = V_{\text{CW}} + V_{\text{c.t.}}. \tag{3.6}$$

Next, we include the one-loop finite temperature correction [48,51]

$$V_{1T}(R, T) = \frac{T^4}{2\pi^2} \sum_i (-1)^{f_i} n_i J_{b/f}\left(\frac{m_i^2}{T^2}\right), \tag{3.7}$$

where the functions $J_{b/f}$ are given by

$$J_{b/f}(x^2) = \int_0^\infty dy\, y^2 \log[1 \mp e^{-\sqrt{y^2 + x^2}}]. \tag{3.8}$$

In the high-T approximation, i.e. $x^2 \equiv \frac{m_i^2}{T^2} \ll 1$, Eq. (3.8) simplifies to [52]

$$J_f(x^2) \approx -\frac{7\pi^4}{360} + \frac{\pi^2}{24} x^2 + \mathcal{O}(x^4),$$

$$J_b(x^2) \approx -\frac{\pi^4}{45} + \frac{\pi^2}{12} x^2 - \frac{\pi}{6} (x^2)^{3/2} + \mathcal{O}(x^4). \tag{3.9}$$

The nonanalytic $(x^2)^{3/2}$ term present in the bosonic case is mainly responsible for the formation of a barrier between

the minima of the effective potential at zero and nonzero field values, leading to a FOPT.

In addition to the one-loop terms, multiloop contributions from daisy diagrams need to be re-summed to cure the infrared divergence arising from the bosonic zero-modes [53]. There are two ways to do this: the Parwani method [54] and the Arnold-Espinosa method [55]. In the Parwani method, the field-dependent mass is replaced with thermally corrected mass, i.e., $m_i^2(R) \to m_i^2(R) + \Pi_i(T)$, in the expressions of V_{CW} and V_{1T}. Here Π_i is the thermal mass obtained using the high-T expansion of V_{1T}, as shown in Appendix B. The daisy re-summed effective potential is given by

$$V_{\text{eff}} = V_0 + V_{CW}(m_i^2(R) + \Pi_i(T)) + V_{\text{c.t.}} \\ + V_{1T}(m_i^2(R) + \Pi_i(T)). \quad (3.10)$$

In the Arnold-Espinosa method, no such replacement for field-dependent mass is made, but an extra daisy term is added to the effective potential:

$$V_D = -\frac{T}{12\pi} \sum_i n_i((m_i^2(R) + \Pi_i(T))^{3/2} - (m_i^2(R))^{3/2}). \quad (3.11)$$

Thus the effective potential is given by

$$V_{\text{eff}} = V_0 + V_{CW} + V_{\text{c.t.}} + V_{1T} + V_D. \quad (3.12)$$

In our analysis, we use the Arnold-Espinosa method, as it takes into account the daisy resummation consistently at the one-loop level, while the Parwani method mixes higher-order loop effects in the one-loop analysis.

IV. PARAMETER SCAN

As discussed earlier, DLRSM has a large number of parameters: ten quartic couplings, along with r, w, μ_4, and v_R. This is called the *generic basis*. To reduce the number of parameters for our analysis, we work in the *simple basis*, introduced in Ref. [36]. The condition of boundedness from below, discussed in Sec. II D, requires that the ratio $x = \lambda_2/\lambda_4$ is restricted to the range $x \in [0.25, 0.85]$. Therefore, we keep λ_2 as a separate parameter, while we equate $\lambda_1 = \lambda_3 = \lambda_4 \equiv \lambda_0$. Similarly, guided by the approximate mass relation, $m_{H_1} \approx \frac{1}{2}(\alpha_3 - \alpha_4)$, we allow for the possibility of having $\alpha_3 \neq \alpha_4$ by keeping them independent, while setting $\alpha_1 = \alpha_2 = \alpha_4 \equiv \alpha_0$. Thus the *simple basis* contains six quartic couplings

$$\{\lambda_0, \lambda_2, \alpha_0, \alpha_3, \rho_1, \rho_2\}. \quad (4.1)$$

Along with these quartic couplings, we also scan over the *vev* ratios r, w, and take $v_R = 20, 30, 50$ TeV. As the mass parameter μ_4 plays an insignificant role in the effective potential, we set $\mu_4 = 0$ in our analysis. Using the *simple basis* allows us to capture the key features of GW phenomenology of DLRSM while retaining the interplay of the existing theoretical and collider constraints.

In preliminary scans, we find that promising scenarios of strong first-order phase transition occur for small values of ρ_1. For points with relatively large couplings, the daisy potential, V_D, given in Eq. (3.11) starts dominating over the contribution from the thermal potential, V_{1T}, given in Eq. (3.7). When this happens, the symmetry-restoring property of the finite temperature effective potential is lost and instead, symmetry nonrestoration is observed. Then the minimum at the nonzero field value becomes deeper at high temperatures, implying the absence of a phase transition, as discussed in Refs. [56–58]. Based on these observations, we choose the following parameter ranges:

$$\log \alpha_0 \in [-3, 0], \quad \log \alpha_3 \in [-3, 0], \quad \log \rho_1 \in [-3.5, -0.5], \quad \rho_2 \in [0, 4\pi],$$
$$x \in [0.25, 0.85], \quad \log r \in [-3, 0], \quad \log w \in [-6, 1], \quad v_R = 20, 30, 50 \text{ TeV}. \quad (4.2)$$

Each parameter is selected randomly from a uniform distribution in the respective range. The parameter λ_0 is chosen in the following manner:

  (i) To increase the number of points satisfying the bound on SM-like Higgs mass (m_h), we solve the equation, $m_{h,\text{analytic}}(\lambda_0 = \Lambda_0) = 125.38$ GeV, for a fixed set of values $\{\alpha_0, \alpha_3, \rho_1, \rho_2, x\}$.

  (ii) Using the solution Λ_0, we choose a random value of λ_0 as, $\lambda_0 = (1 + y)\Lambda_0$, with $y \in [-0.1, 0.1]$.

  (iii) Finally, each parameter point is defined by the set:

$$\{\lambda_0, \lambda_2 = x\lambda_0, \alpha_0, \alpha_3, \rho_1, \rho_2, r, w, v_R\}$$

Given a parameter point, we first check if it satisfies the theoretical constraints: boundedness from below, perturbativity, and unitarity, discussed in Sec. II D. Next, the Higgs constraints described in Sec. II E are checked. Furthermore, the constraint from meson mixing $m_{H_1} > 15$ TeV is imposed.
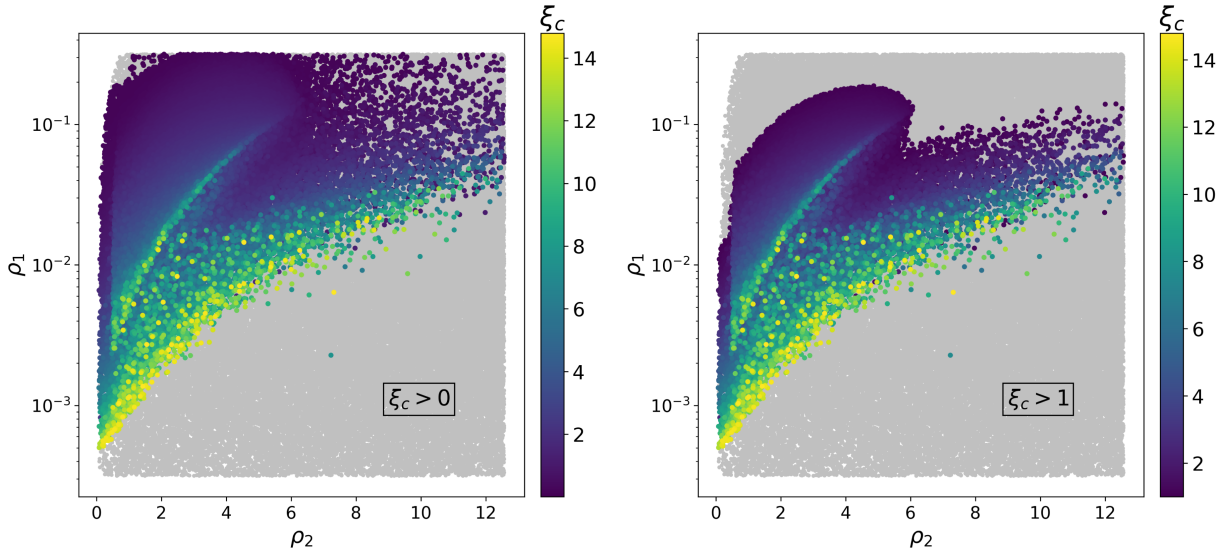
FIG. 1. Points with strong FOPT in the ρ_1–ρ_2 plane, for $v_R = 30$ TeV. The gray points have passed the theoretical and experimental constraints. The left panel shows all points showing FOPT with $\xi_c > 0$, whereas in the right panel, the points satisfy the condition $\xi_c > 1$.

If the parameter point passes all the aforementioned theoretical and experimental constraints, we construct the effective potential using the Arnold-Espinosa method. We satisfy the Linde-Weinberg bound [59,60] by numerically checking that the minimum of the zero-temperature effective potential at $R = v_R$ is the absolute minimum. We reject the point if symmetry nonrestoration persists at high temperatures. Next, we check for a possible first-order phase transition, using the python-based package COSMOTRANSITIONS [61]. The strength of FOPT can be quantified by the ratio

$$\xi_c = \frac{v_c}{T_c}, \qquad (4.3)$$

where T_c is the critical temperature at which the two minima become degenerate and v_c is the *vev* at T_c. The FOPT is considered to be strong if the following criterion is met [62],[1]

$$\xi_c > 1. \qquad (4.4)$$

In Fig. 1, we show the points with FOPT projected onto the ρ_1–ρ_2 plane for $v_R = 30$ TeV, color-coded according to the value of ξ_c. The left panel shows all points with $\xi_c > 0$, while the right panel only shows points satisfying the SFOPT criterion $\xi_c > 1$. The gray dots depict parameter

points passing the existing theoretical and experimental bounds. As suggested by the preliminary scans, SFOPT prefers $\rho_1 \lesssim \mathcal{O}(0.1)$. Points with $\rho_1 \lesssim \mathcal{O}(10^{-2})$ and $\rho_2 \gtrsim \mathcal{O}(1)$ violate the Linde-Weinberg bound. Therefore, there are no points showing SFOPT in this region. A large number of points with $\rho_2 \gtrsim 6$ also exhibit symmetry nonrestoration at high temperatures.

Figure 2 shows various two-dimensional projections of the DLRSM parameter space for $v_R = 30$ TeV, depicting points with SFOPT. The parameter α_0 is always smaller than 1, as indicated by the left panels in the top and the bottom row. We also restrict ourselves to $\alpha_3 < 1$ to avoid points showing symmetry nonrestoration. Along the α_3 direction, there is a sharp change in the density of points around $\alpha_3 \approx 0.5$, coming from the bound $m_{H_1} > 15$ TeV. The value of α_3 where the density changes is different for $v_R = 20, 30,$ and 50 TeV. Since the couplings are small for a large number of parameter points, the approximate relation given in Eq. (2.11) tells us that λ_1 can take values close to $\lambda_{SM} \approx 0.13$. In the top right and bottom left panels, we indeed observe an overdensity of points clustered around $\lambda_0 \approx 0.13$. In the ρ_1–λ_0 plane, a majority of points with large ξ_c occur for small ρ_1, and large λ_0. In the r–w plane, points with large ξ_c occur mostly at higher values of w [$\gtrsim \mathcal{O}(0.1)$] and are less frequent for smaller values of w. So this parameter region can lead to a detectable GW background. There is no preference along the r direction. The points with large ξ_c also have relatively large values of y_{33}, as indicated by the contours corresponding to $y_{33} = 1,$ 1.5, and $\sqrt{4\pi}$.

The strength of FOPT is more rigorously characterized by three parameters, $\alpha, \beta/H_*,$ and T_n, which are required to compute the GW spectrum. These are defined as follows:

---

[1]It is known that the field value, v_c, and T_c are gauge dependent, therefore, so is the ratio $\frac{v_c}{T_c}$. However changing the gauge-fixing parameter has a subleading effect on $\frac{v_c}{T_c}$ [63,64]. In the subsequent analysis, we work in the Landau gauge, for which the gauge-dependence is numerically minimized.
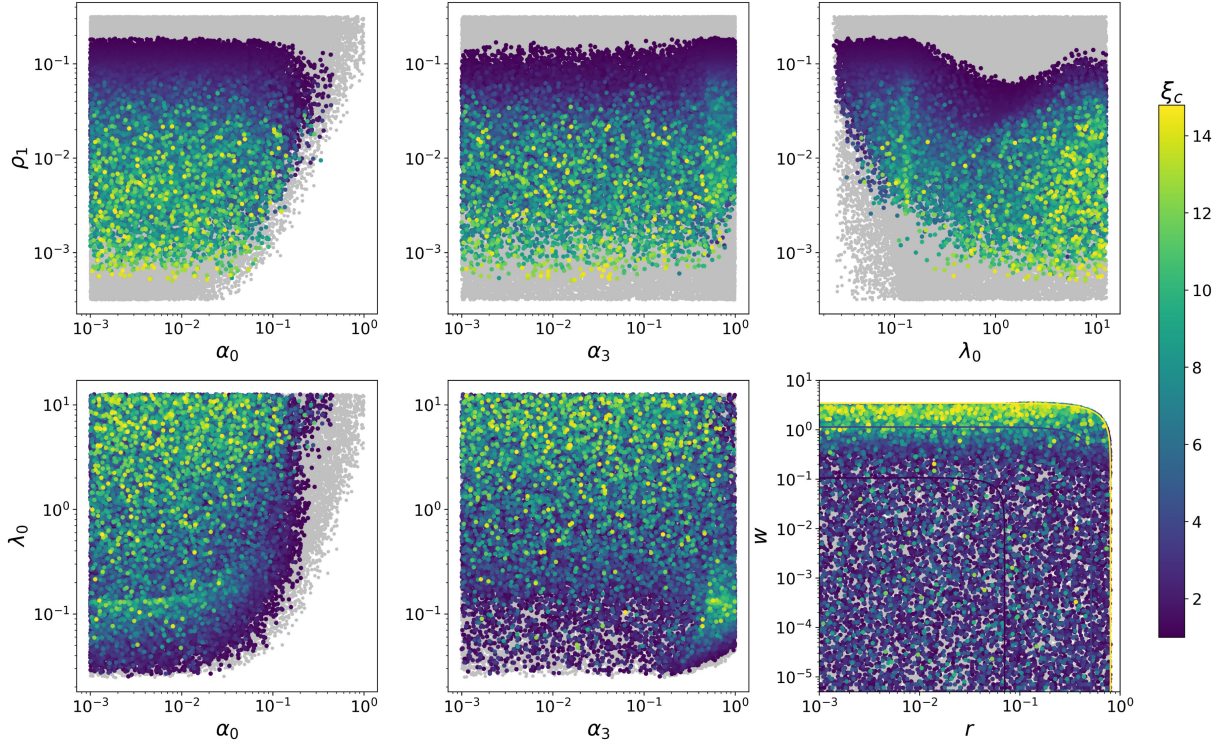
FIG. 2. Projections showing the points with SFOPT on different parameter planes, for $v_R = 30$ TeV. The gray points show all points passing the theoretical and experimental constraints. The points satisfy the condition $\xi_c > 1$.

(i) The probability of tunneling from the metastable to the stable minimum is given by [65]

$$\Gamma(T) \approx T^4 \left(\frac{S_3}{2\pi T}\right)^{3/2} e^{-\frac{S_3}{T}}, \qquad (4.5)$$

where S_3 is the $O(3)$-symmetric Euclidean bounce action. This is calculated using the tunneling solution of the equation of motion of the scalar field. We use COSMOTRANSITIONS [61] to compute S_3. The probability of nucleating a bubble within a Hubble volume increases as the universe cools below T_c, and becomes $\mathcal{O}(1)$ at the nucleation temperature, T_n. This happens when

$$\Gamma(T_n) \approx (H(T_n))^4. \qquad (4.6)$$

In the radiation-dominated era, this implies [66]

$$\frac{S_3(T_n)}{T_n} \simeq -4 \ln\left(\frac{T_n}{m_{\text{Pl}}}\right), \qquad (4.7)$$

where the Planck mass $m_{\text{Pl}} = 1.22 \times 10^{19}$ GeV.

(ii) The parameter α is the vacuum energy released during the transition, ρ_{vac}, normalized by the radiation density at the time of FOPT [67],

$$\alpha \equiv \frac{\rho_{\text{vac}}}{\rho_{\text{rad}}}, \qquad (4.8)$$

where,

$$\rho_{\text{vac}} = (V_{\text{High}} - V_{\text{Low}}) - \frac{T}{4}\left(\frac{\partial V_{\text{High}}}{\partial T} - \frac{\partial V_{\text{Low}}}{\partial T}\right)\bigg|_{T=T_*}, \qquad (4.9)$$

$$\rho_{\text{rad}} = \frac{\pi^2}{30} g_* T_*^4. \qquad (4.10)$$

Here T_* is the temperature of the universe at the time when dominant GW production takes place. We take $T_* \simeq T_n$ in our calculations. The subscripts "High" and "Low" refer to the metastable and stable minima respectively, at the time of tunneling. g_* is the number of relativistic degrees of freedom at $T = T_*$. For DLRSM, $g_* = 130$.

(iii) β is related to the rate or inverse duration of the phase transition, defined as [25]

$$\beta \equiv -\frac{dS}{dt}\bigg|_{t=t_*} = TH_*\frac{dS}{dT}\bigg|_{T=T_*}, \qquad (4.11)$$

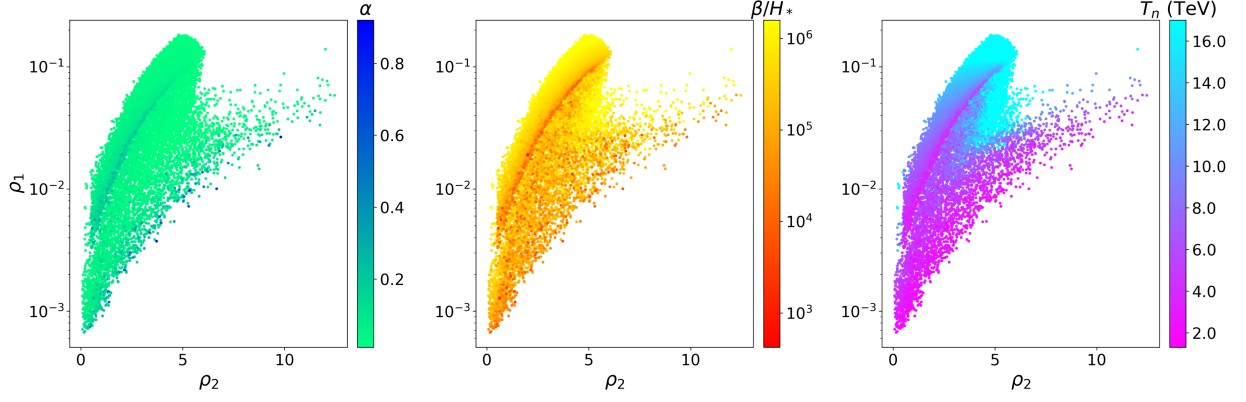where, $S = S_3/T$ and H_* is the Hubble's constant at $T = T*$.

FIG. 3. Variation of PT parameters in the ρ_1–ρ_2 plane. Color code shows the variation of α (left), β/H_* (middle), and T_n (right). Here, $v_R = 30$ TeV.

For points satisfying $\xi_c > 1$, we compute the nucleation temperature T_n. We find the solution of Eq. (4.7) using the secant method, where the tunneling action is calculated by COSMOTRANSITIONS. We remove any points with $T_n < 0$, as this indicates that the PT is not completed till the present time. Moreover, we set a lower bound of $T_n > 500$ GeV to ensure that the PT is completed before the EW epoch. Once T_n is obtained, α and β/H_* can be computed using Eqs. (4.8) and (4.11) respectively. Figure 3 shows the variation of the PT parameters α (left panel), β/H_* (middle panel), and T_n (right panel), in the ρ_1–ρ_2 plane. The evaluated ranges roughly are, $\alpha \in [0, 0.8]$, $\beta/H_* \in [10^2, 10^6]$, and $T_n \in [2, 16]$ TeV. T_n is observed to take smaller values in regions where the strength of SFOPT is high.

V. GRAVITATIONAL WAVE BACKGROUND

The GW spectrum is defined as [25]

$$\Omega_{\rm GW}(f) \equiv \frac{1}{\rho_c} \frac{d\rho_{\rm GW}}{d \ln f}, \tag{5.1}$$

where f is the frequency, $\rho_{\rm GW}$ is GW energy density, and ρ_c is the critical energy density of the universe, given by,

$$\rho_c = \frac{3H_0^2}{8\pi G}. \tag{5.2}$$

Here, $H_0 = 100h \; {\rm km \, s^{-1} \, Mpc^{-1}}$ is the Hubble constant with the current value of $h = 0.6736 \pm 0.0054$ [68] and G is Newton's gravitational constant.

A strong FOPT proceeds by nucleation of bubbles of the stable phase which expand rapidly in the sea of the metastable phase. GWs are produced when the expanding bubbles collide and coalesce with each other. If sufficient friction exists in the plasma, the bubble walls may reach a terminal velocity v_w. We take $v_w = 1$ in our analysis. GW production happens via three main processes: bubble wall collisions ($\Omega_{\rm col}$), sound waves produced in the thermal plasma ($\Omega_{\rm sw}$), and the resulting MHD turbulence ($\Omega_{\rm turb}$). For a recent review of the different GW production mechanisms, please refer to [26]. In the nonrunaway scenario [25], GW production happens primarily through sound waves and turbulence, i.e.,

$$h^2\Omega_{\rm GW} \simeq h^2\Omega_{\rm sw} + h^2\Omega_{\rm turb}, \tag{5.3}$$

where [25,69],

$$h^2\Omega_{\rm sw}(f) = 2.65 \times 10^{-6} \left(\frac{100}{g_*}\right)^{1/3} \left(\frac{H_*}{\beta}\right)^2$$
$$\times \left(\frac{\kappa_{\rm sw}\alpha}{1+\alpha}\right)^2 v_w S_{\rm sw}(f)\Upsilon(\tau_{\rm sw}), \tag{5.4}$$

$$h^2\Omega_{\rm turb}(f) = 3.35 \times 10^{-4} \left(\frac{100}{g_*}\right)^{1/3} \left(\frac{H_*}{\beta}\right)^2$$
$$\times \left(\frac{\kappa_{\rm turb}\alpha}{1+\alpha}\right)^{3/2} v_w S_{\rm turb}(f). \tag{5.5}$$

Here, $\kappa_{\rm sw}$ and $\kappa_{\rm turb}$ are the efficiency factors for the respective processes. The efficiency factor $\kappa_{\rm sw}$ is given by

$$\kappa_{\rm sw} = \frac{\alpha}{0.73 + 0.083\sqrt{\alpha} + \alpha}, \tag{5.6}$$

and $\kappa_{\rm turb}$ is known to be at most 5–10% of $\kappa_{\rm sw}$. Here we take $\kappa_{\rm turb} = 0.05\kappa_{\rm sw}$. We have included the suppression factor $\Upsilon(\tau_{\rm sw})$ that arises due to the finite lifetime $\tau_{\rm sw}$ of sound waves [69],

$$\Upsilon(\tau_{\rm sw}) = 1 - \frac{1}{\sqrt{1 + 2\tau_{\rm sw}H_*}}, \tag{5.7}$$

with

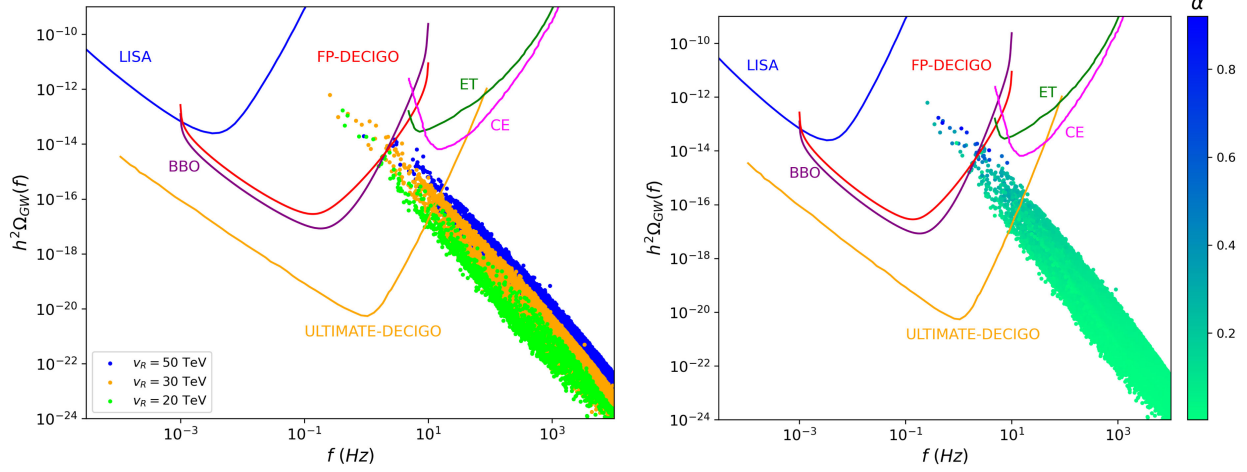$$\tau_{\rm sw} = \frac{R_*}{\overline{U}_f}, \tag{5.8}$$

FIG. 4. The peak of the GW spectrum $\Omega_{\rm GW}$ for points with SFOPT, along with the power-law integrated sensitivity curves of various upcoming GW detectors. Left: points corresponding to $v_R = 20$, 30, and 50 TeV are shown. Right: Points are color-coded according to the value of α, for $v_R = 20$, 30, and 50 TeV combined.

where the mean bubble separation $R_* \simeq (8\pi)^{1/3} v_w/\beta$ and the mean square velocity is

$$\overline{U_f}^2 = \frac{3}{4}\frac{\alpha}{1+\alpha}\kappa_{\rm sw}. \qquad (5.9)$$

The spectral shape functions, $S_{\rm sw}$ and $S_{\rm turb}$ determine the behavior of each contribution at low and high frequencies. These are

$$S_{\rm sw}(f) = \left(\frac{f}{f_{\rm sw}}\right)^3 \left(\frac{7}{4+3(f/f_{\rm sw})^2}\right)^{7/2},$$

$$S_{\rm turb}(f) = \left(\frac{f}{f_{\rm turb}}\right)^3 \frac{1}{[1+(f/f_{\rm turb})]^{11/3}(1+8\pi f/h_*)}. \qquad (5.10)$$

Here, h_* is the Hubble rate at $T = T_*$,

$$h_* = 1.65 \times 10^{-7}~{\rm Hz}\left(\frac{T_*}{100~{\rm GeV}}\right)\left(\frac{g_*}{100}\right)^{1/6}. \qquad (5.11)$$

The redshifted peak frequencies, after taking into account the expansion of the universe, are,

$$f_{\rm sw} = 1.9 \times 10^{-5}~{\rm Hz}\left(\frac{g_*}{100}\right)^{1/6}\frac{1}{v_w}\left(\frac{\beta}{H_*}\right)\left(\frac{T_*}{100~{\rm GeV}}\right), \qquad (5.12)$$

$$f_{\rm turb} = 2.7 \times 10^{-5}~{\rm Hz}\left(\frac{g_*}{100}\right)^{1/6}\frac{1}{v_w}\left(\frac{\beta}{H_*}\right)\left(\frac{T_*}{100~{\rm GeV}}\right). \qquad (5.13)$$

From the expressions of $\Omega_{\rm sw}$ and $\Omega_{\rm turb}$, it is clear that large α and small β/H_* lead to a strong GW spectrum. The peak frequency is proportional to $T_n \sim v_R$ and hence, the peak shifts to the right for larger v_R. This is illustrated in Fig. 4, where we show scatter plots of the parameter points for which α, β/H_*, and T_n have been computed. Each point represents the peak value corresponding to the GW spectrum, $h^2\Omega_{\rm GW}$. The left panel shows that these points shift to the right as v_R is progressively increased between $v_R = 20$, 30 and 50 TeV. The strength of the GW signature is not affected by varying v_R. The right panel shows the variation of α for the points corresponding to $v_R = 20$, 30, and 50 TeV combined. There is clearly a positive correlation between large α and the strength of GW. The solid lines represent the power-law integrated sensitivity curves [70] corresponding to various planned detectors calculated for an observation time of $\tau = 1$ year, and a threshold SNR $= 1$ [see Eq. (6.1)]. The curve for Ultimate-DECIGO is obtained following the prescription of Ref. [71], while the other curves are taken from [72]. Points lying above the sensitivity curve of a detector feature SNR > 1, and have strong detection prospects. The DLRSM phase transition has good detection prospects for the detectors FP-DECIGO, BBO, and Ultimate-DECIGO for the chosen set of v_R values. The GW spectrum is too weak to be detected at ET and CE for the chosen range of v_R. If the scale v_R is increased by a factor of $\sim$10–100, these two detectors may be able to detect them, but we ignore this region as the complementary collider constraints would be too weak.

In Fig. 5 we illustrate the distribution of the points with detectable GW signal in the r–w plane. The gray points pass all the theoretical and experimental constraints. The blue points are only detectable at Ultimate-DECIGO, the green points are detectable by Ultimate-DECIGO as well as BBO, and the red points can be detected at all three detectors.
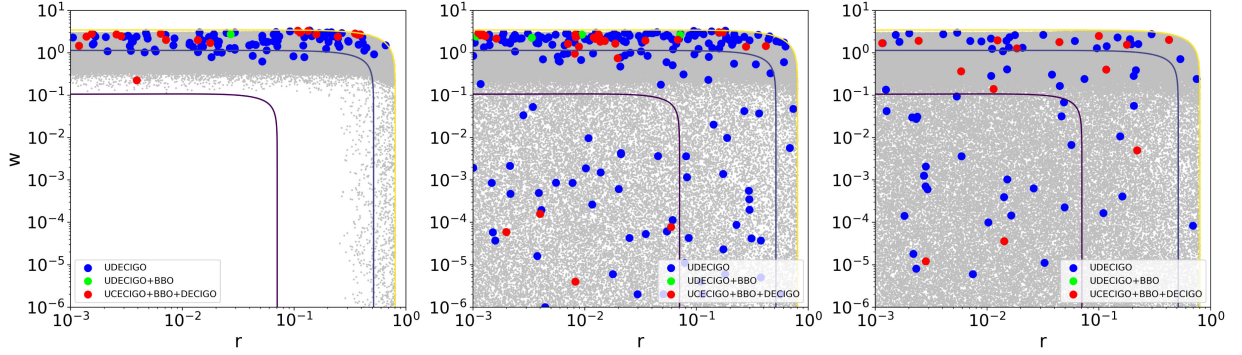
FIG. 5. Points with detectable GW signature at upcoming observatories: Ultimate-DECIGO (UDECIGO), BBO, and FP-DECIGO. The scale is chosen to be, $v_R = 20$ TeV (left), $v_R = 30$ TeV (middle), and $v_R = 50$ TeV (right). The purple, blue, and yellow contours represent the upper limits on $y_{33} = 1, 1.5, \sqrt{4\pi}$ respectively based on Eq. (2.15).

Interestingly, for $v_R = 20$ TeV, the red, green, and blue points are densely clustered around $w \sim \mathcal{O}(1)$. For most of these points, y_{33} is also large, $y_{33} \sim 1.5 - \sqrt{4\pi}$. In the middle panel, i.e. $v_R = 30$ TeV, the majority of points still prefer $w \sim \mathcal{O}(1)$, but now there are also points at lower values of w. In the case of $v_R = 50$ TeV, we see that the clustering of points around $\mathcal{O}(1)$ values of w is even more diffuse. In all three cases, i.e., $v_R = 20$, 30, and 50 TeV, there is no particular preference in the r direction, as also seen from the SFOPT plots given in Fig. 2.

VI. DETECTION PROSPECTS

The prospect of detecting a GW signal in a given GW observatory can be quantified using the signal-to-noise ratio (SNR), defined as [26,70]

$$\text{SNR} = \sqrt{n_{\text{det}}\tau \int_{f_{\min}}^{f_{\max}} df \left[\frac{\Omega_{\text{GW}}(f)h^2}{\Omega_{\text{sens}}(f)h^2}\right]^2}, \quad (6.1)$$

where τ is the time period (in seconds) over which the detector is active, and the integration is carried out over the entire frequency range $[f_{\min}, f_{\max}]$ of the detector. For calculations, we take $\tau = 1$ year. The factor n_{det} is two for experiments aimed at GW detection via cross-correlation measurement, or one for experiments aimed at detection via auto-correlation measurement (e.g., LISA). $\Omega_{\text{sens}}(f)$ is the noise energy density power spectrum for the chosen detector. A signal is detectable if the observed SNR value exceeds a threshold SNR, denoted as $\text{SNR}_{\text{thres}}$. The value of $\text{SNR}_{\text{thres}}$ varies from detector to detector. We take $\text{SNR}_{\text{thres}} = 1$ for the purpose of discussion.

TABLE I. Benchmark points for DLRSM in the simple basis.

|	BP1	BP2	BP3	BP4	BP5	BP6
v_R (TeV)	30	30	30	30	20	50
λ_0	0.126796	0.466090	0.308396	0.324564	1.982649	0.799371
λ_2	0.097015	0.253725	0.141320	0.267655	1.670007	0.413236
α_0	0.004789	0.003504	0.007640	0.012450	0.012042	0.021020
α_3	0.957421	0.005786	0.006466	0.004839	0.001015	0.003094
ρ_1	0.019071	0.001274	0.001929	0.005930	0.009976	0.003445
ρ_2	2.003479	0.627225	1.166146	1.674371	5.574184	2.275937
r	0.008261	0.008136	0.418869	0.020970	0.390416	0.424048
w	4×10^{-6}	0.950364	1.439902	0.766492	2.702912	2.018973
$m_{W_R^\pm}$ (TeV)	9.81	9.81	9.81	9.81	6.54	16.35
m_{Z_R} (TeV)	11.58	11.58	11.58	11.58	7.72	19.30
m_{H_1} (TeV)	20.72	15.97	32.79	20.89	81.06	99.90
m_{H_2} (TeV)	29.74	23.13	45.58	34.46	116.99	144.97
m_{H_3} (TeV)	5.86	1.51	1.86	3.27	2.82	4.15
α	0.280	0.274	0.243	0.122	0.428	0.273
β/H_*	422	1050	2648	8267	975	3204
T_c (TeV)	5.78	3.26	3.46	4.83	2.82	5.87
T_n (TeV)	3.08	1.68	1.86	2.91	1.37	3.26
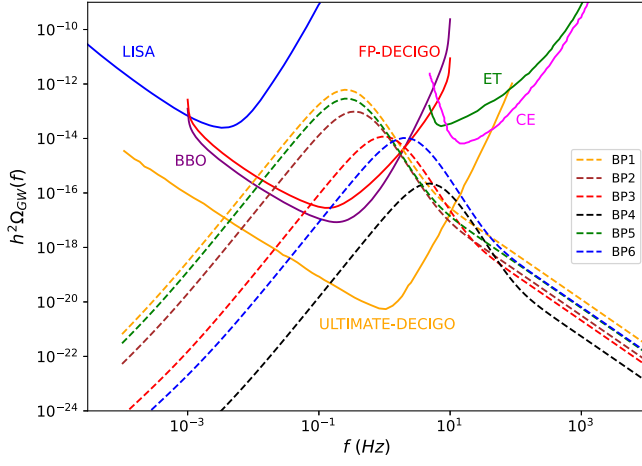
FIG. 6. GW spectra for the benchmark points listed in table I.

Table I presents six benchmark points (BP) with high SNR values for FP-DECIGO, BBO, and Ultimate-DECIGO, obtained using Eq. (6.1). BP1, BP2, BP3, and BP4 have been chosen at the $SU(2)_R$ breaking scale $v_R = 30$ TeV, while for BP5 and BP6 the chosen scales are $v_R = 20$ TeV and 50 TeV respectively. The top segment of the table shows the values of the quartic couplings, while the middle segment gives the mass spectrum corresponding to each BP. The bottom segment gives the values of PT parameters α, β/H_*, T_c and T_n. Barring BP1, all other BPs have $w \sim \mathcal{O}(1)$. All BPs have $\rho_1 \lesssim \mathcal{O}(10^{-1})$ and hence smaller values of m_{H_3} are preferred.

The full GW spectra for the BPs are shown in Fig. 6. The peak of the spectrum corresponds to the frequency f_{sw} defined in Eq. (5.12) since Ω_{sw} gives the dominant contribution. The peak of BP4 lies only above Ultimate-DECIGO and below BBO and FP-DECIGO, while all other BPs have GW peaks above the sensitivity curves of Ultimate-DECIGO, BBO, and FP-DECIGO. The low- and high-frequency tails are dominated by the power law behavior of Ω_{turb}.

The SNR of the BPs are listed in Table II. As proclaimed in the previous section, the BPs generally yield high SNR values for FP-DECIGO, BBO, and Ultimate-DECIGO. The SNR values for BP1, BP2, BP3, BP5, and BP6 are higher than 1 for FP-DECIGO, BBO, and Ultimate-DECIGO, and hence have good detection prospects. Ultimate-DECIGO, being the most sensitive, can detect all the BPs listed in Table II with large SNR values $> 10^4$. The point BP4 is not

detectable at FP-DECIGO and BBO, but can be detected by Ultimate-DECIGO.

VII. COMPLEMENTARY COLLIDER PROBES

Now we describe the collider probes that complement the GW signatures discussed in the previous sections. We discuss two important collider implications, namely the precision of κ_h and detection of H_3.

(i) As argued in Sec. II E, in DLRSM the trilinear Higgs coupling can deviate significantly from its SM value. In Table III, we present the percentage of points leading to detectable GW signal at Ultimate-DEC-IGO, which also show deviation of κ_h at 5%, 10%, 20%, and 50%. The current ATLAS measurement allows for a rather large range of $\kappa_h \in [-2.3, 10.3]$. However, future colliders will significantly tighten the bound. Here we quote the projected sensitivities of κ_h from Ref. [73]. HL-LHC will achieve a sensitivity of 50% from the di-Higgs production channel. The proposed colliders, such as HE-LHC, CLIC$_{3000}$, and FCC-hh are expected to improve the sensitivity of κ_h to $\sim 20\%$, 10%, and 5% respectively. These colliders therefore will rule out a considerable number of points showing a strong GW signal.

(ii) The scalar H_3 can be produced at pp colliders through several channels, for example [43],
(a) H_1-decay, $pp \to H_1 \to hH_3$,
(b) decay of boosted h, $pp \to h^* \to hH_3, H_3H_3$,
(c) Higgsstrahlung, $pp \to V_R^* \to V_R H_3$,
(d) $V_R V_R$ fusion, $pp \to H_3 jj$.

The relative strength of these processes depends on the mass spectrum of DLRSM. In Fig. 7, we show the distribution of SFOPT points in the m_{H_1}–m_{H_3} plane for $v_R = 20$ TeV, overlaid with points which are detectable at Ultimate-DECIGO, BBO, and FP-DECIGO. The detectable points mostly occur for small m_{H_3}, with the minimum value of $m_{H_3} = 741$ GeV. For the range $m_{H_3} = 740$ GeV -1.2 TeV, the production cross-section of H_3 at FCC-hh with $\sqrt{s} = 100$ TeV can be $\sim \mathcal{O}(fb)$ [43].

For $v_R = 20$ TeV, $m_{H_3} \lesssim 500$ GeV can be ruled out from the observations of the channel (iv) at FCC-hh with a luminosity of 30 ab^{-1}. For large values of quartic couplings, the decay width $h^* \to hH_3$ and $h^* \to H_3H_3$ can be large and subsequently, channel (ii) can rule out $m_{H_3} \lesssim 700$ GeV. For channel (i), H_1 with mass 15 TeV can be produced with a cross section ~ 0.5 fb and have

TABLE II. SNR values corresponding to different detectors for the benchmark points.

SNR	BP1	BP2	BP3	BP4	BP5	BP6
FP-DECIGO	6.5×10^3	736.0	14.4	6.5×10^{-3}	3.0×10^3	2.4
BBO	5.4×10^4	7.0×10^3	174.2	6.5×10^{-2}	2.5×10^4	28.2
Ultimate-DECIGO	1.2×10^9	2.6×10^8	2.9×10^7	2.2×10^4	6.0×10^8	8.0×10^6

TABLE III. Percentage of points detectable at Ultimate-DEC-IGO to be ruled out when the sensitivity of κ_h reaches 5%, 10%, 20%, and 50%, for $v_R = 20$, 30, and 50 TeV.

$\delta\kappa_h$	20 TeV	30 TeV	50 TeV	Combined
> 5%	52%	58%	50%	54%
> 10%	21%	34%	33%	30%
> 20%	8%	20%	25%	17%
> 50%	1.3%	12%	15%	9%

sizable branching ratios of $H_1 \to hH_3, H_3H_3$. As a result, channel (i) can rule out masses up to $m_{H_3} \sim 2$ TeV. Thus, these searches are capable of ruling out a large number of points with low-m_{H_3}, thus low-ρ_1, providing a complementarity to the GW probe of DLRSM.

VIII. SUMMARY AND CONCLUSIONS

In this paper, we studied the possibility of an observable stochastic GW background resulting from SFOPT associated with the spontaneous breaking of $SU(2)_R \times U(1)_{B-L}$ in DLRSM. The gauge symmetry of DLRSM breaks in the following pattern:

$$SU(2)_L \times SU(2)_R \times U(1)_{B-L} \xrightarrow{v_R} SU(2)_L$$
$$\times U(1)_Y \xrightarrow{\kappa_1, \kappa_2, v_L} U(1)_Y.$$

The nonobservation of a right-handed current at colliders puts a lower bound on the scale v_R to be around 20 TeV.
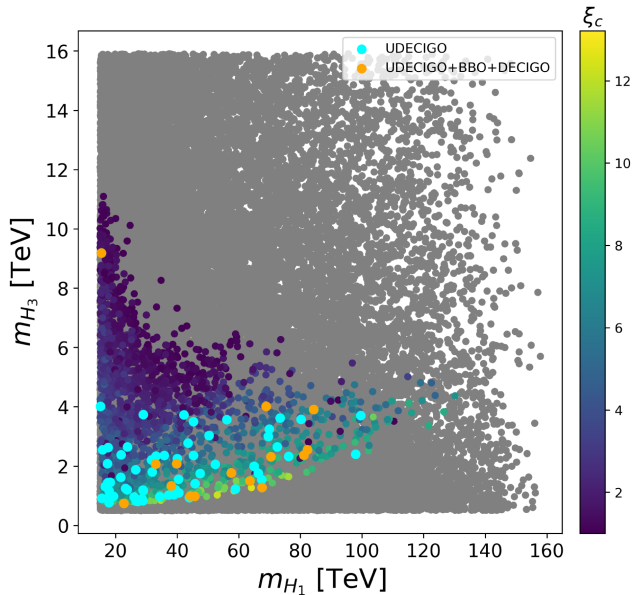

FIG. 7. The mass spectrum of DLRSM for $v_R = 20$ TeV depicting points with $\xi_c > 1$. The cyan and orange points lead to a GW signal detectable at Ultimate-DECIGO and Ultimate-DECIGO+BBO+FP-DECIGO respectively.

Due to the hierarchy $v_R \gg v$, the $SU(2)_R \times U(1)_{B-L}$-breaking dynamics is decoupled from the EWPT. We chose the scale $v_R = 20$, 30, and 50 TeV to study the possible detection of GW background at the planned observatories. For these values of v_R, complementary searches for new scalars of DLRSM are feasible at future colliders.

Our analysis was carried out using the *simple basis* defined in Ref. [36], to reduce the number of independent parameters. It should be noted that analysis with the full set of parameters also gives similar patterns of SFOPT in the $\rho_1 - \rho_2$ and r–w planes. The parameters in the *simple basis* include the quartic couplings: $\lambda_0, \lambda_2, \alpha_0, \alpha_3, \rho_1, \rho_2$. In addition, we defined EW *vevs* through the ratios r and w. Most studies on LRSM take the simplified limit $r, w \to 0$. However, it was pointed out in Refs. [35,36] that the DLRSM phenomenology allows for significant deviation from this limit. Therefore, we also scanned over r and w.

We constructed the one-loop finite temperature effective potential for each parameter point and analyzed the nature of PT using the package COSMOTRANSITIONS. Due to the large separation between v_R and the EW scale, the effective potential depends solely on the background field value of the neutral CP-even scalar, χ^0_{Rr}. The condition for SFOPT, $\xi_c > 1$ was used to identify viable regions of the parameter space. SFOPT favors small values of the quartic coupling $\rho_1 \lesssim \mathcal{O}(10^{-1})$, which leads to $m_{H_3} \ll v_R$. This feature has also been observed in other variants of LRSM, discussed in Refs. [17,32,33].

We find that for very small values, $\rho_1 \lesssim 10^{-3}$ however, the zero temperature minimum of the one-loop effective potential at $R = v_R$ becomes metastable, violating the Linde-Weinberg bound. Hence there is a lower bound on ρ_1 below which FOPT is not observed. Most points with SFOPT also feature $w \sim \mathcal{O}(1)$, while for smaller values of w, very few points show SFOPT. Out of the chosen set of parameters, the SFOPT region is most sensitive to the parameters ρ_1 and w and to some extent λ_0. However, we see no particular preference for the *vev* ratio r and the quartic couplings relating the bidoublet and the doublet fields, i.e., α_0 and α_3, as illustrated by the projections given in Fig. 2.

For parameter points showing SFOPT, we computed the PT parameters, $\alpha, \beta/H_*$, and T_n, needed for the calculation of the GW spectrum. In the nonrunaway scenario, the stochastic GW background resulting from SFOPT comes primarily from sound waves and turbulence, while the contribution from bubble wall collisions remains subdominant. Figure 4 shows the position of the peak of the GW spectrum for points satisfying the SFOPT criterion. While for a large number of points, the GW spectrum is too weak to be detected, there is a significant number of points lying above the sensitivity curves for Ultimate-DECIGO, BBO, and FP-DECIGO. Such points will be accessible to these detectors in the coming years. The detectable points

also prefer $w \sim \mathcal{O}(1)$, which in turn, correspond to a large value of y_{33} as seen in Fig. 5.

The strength of the GW spectrum does not depend on the scale v_R. On the other hand, since the peak frequency is proportional to $T_n \sim v_R$, the points shift to the right as v_R changes from 20 to 30 to 50 TeV. To quantify the detection prospects, we computed the signal-to-noise ratio at these detectors for the detectable points. Six benchmark points are given in Table II, featuring SNR values higher than 10^5. We see that for all the BPs, $m_{H_3} \lesssim 5$ TeV.

There are primarily two complementary collider probes for the points with detectable GW signals. It was found that a significant fraction of points leads to 50%, 20%, 10%, and 5% deviation of k_h from unity, which can be ruled out at HL-LHC, HE-LHC, CLIC$_{3000}$, and FCC-hh respectively. Due to a relatively low mass of H_3, it can be produced at future colliders through various channels. In particular, FCC-hh can rule out up to $m_{H_3} \sim 2$ TeV.

Here we make a note of some subtleties involved in computing the GW spectrum that contribute to theoretical uncertainty: (i) The suppression factor Υ, introduced in (5.4) was recently proposed, to take the finite lifetime of sound waves into account. For the chosen benchmark points this suppression factor takes $\mathcal{O}(0.1)$ values. (ii) As pointed out earlier, the value of v_c/T_c depends on the particular choice of gauge since the effective potential is gauge dependent. The effect of gauge-dependence in minimized in the Landau gauge, which we use for our calculations. (iii) In principle, the bubble wall velocity can be computed from the model parameters, as seen in Refs. [74–76]. We use $v_w = 1$, which is valid when the friction on the walls is low. Thus a particular choice of v_w

can cause small shifts in the GW spectrum. We checked that the uncertainties mentioned above contribute to roughly $\mathcal{O}(0.1–1)$ deviations in the GW spectrum of the BPs. However, the BPs would still be detectable at respective detetectors, BBO and/or DECIGO.

The spontaneous breaking of the discrete LR symmetry $\mathcal{P}$ can lead to the formation of domain walls. The GW imprint from the domain wall network peaks at much lower frequencies, as compared to that from FOPT [34,41]. Since there is no overlap of the GW signals, we have focussed our discussion on FOPT.

Although DLRSM does not account for neutrino masses, it is interesting to ask if incorporating them by adding extra fields to the model could modify the strength of FOPT. In Appendix C, we have shown that it is possible to include neutrino masses without impacting the results of our analysis.

APPENDIX A: MINIMIZATION AT THE EW VACUA

The minimization conditions are given by:

$$\mu_1^2 = \frac{1}{2(r^2-1)}(\kappa_1^2(w^2((r^2-1)\alpha_1 + r^2\alpha_3 - \alpha_4) + 2(r^2-1)((r^2+1)\lambda_1 + 2r\lambda_4))$$
$$+ 2\sqrt{2}rv_R w\mu_4 + v_R^2((r^2-1)\alpha_1 + r^2\alpha_3 - \alpha_4 + 2w^2\rho_{12})),$$
$$\mu_2^2 = \frac{1}{4(r^2-1)}(\kappa_1^2(w^2(r^2-1)\alpha_2 - w^2 r\alpha_{34} + 2(r^2-1)(2r\lambda_{23} + (r^2+1)\lambda_4))$$
$$- \sqrt{2}(r^2+1)v_R w\mu_4 + v_R^2((r^2-1)\alpha_2 - r\alpha_{34} - 2w^2\rho_{12})),$$
$$\mu_3^2 = \frac{1}{2}\kappa_1^2((r^2+1)\alpha_1 + 2r\alpha_2 + r^2\alpha_3 + \alpha_4 + 2w^2\rho_1) + v_R^2\rho_1,$$
$$\mu_5 = -r\mu_4 - \sqrt{2}v_R w\rho_{12}, \tag{A1}$$

where, $\rho_{12} = \rho_2/2 - \rho_1$, $\alpha_{34} = \alpha_3 - \alpha_4$, and $\lambda_{23} = 2\lambda_2 + \lambda_3$.

APPENDIX B: FIELD-DEPENDENT MASSES

The field-dependent mass matrices are obtained from the tree-level effective potential:

$$m_{ij}^2(R) = \frac{\partial^2}{\partial\varphi_i \partial\varphi_j} V_0 \bigg|_{\langle\cdots\rangle} \tag{B1}$$

where $\langle\cdots\rangle$ denotes the background field value. This amounts to replacing $v_R \to R$, and $\kappa_1, \kappa_2, v_L \to 0$ in the usual mass matrices.

For the *CP*-even sector, in the basis $\{\phi_{1r}^0, \phi_{2r}^0, \chi_{Lr}^0, \chi_{Rr}^0\}$, we obtain,

$$\mathcal{M}_{\text{CPE}}^2 = \begin{pmatrix} -\mu_1^2 + \frac{1}{2}(\alpha_1 + \alpha_4)R^2 & -2\mu_2^2 + \frac{1}{2}\alpha_2 R^2 & \frac{1}{\sqrt{2}}\mu_5 R & 0 \\ -2\mu_2^2 + \frac{1}{2}\alpha_2 R^2 & -\mu_1^2 + \frac{1}{2}(\alpha_1 + \alpha_3)R^2 & \frac{1}{\sqrt{2}}\mu_4 R & 0 \\ \frac{1}{\sqrt{2}}\mu_5 R & \frac{1}{\sqrt{2}}\mu_4 R & -\mu_3^2 + \frac{1}{2}\rho_2 R^2 & 0 \\ 0 & 0 & 0 & -\mu_3^2 + 3\rho_1 R^2 \end{pmatrix}. \tag{B2}$$

For the *CP*-odd scalars, in the basis $\{\phi_{1i}^0, \phi_{2i}^0, \chi_{Li}^0, \chi_{Ri}^0\}$,

$$\mathcal{M}_{\text{CP0}}^2 = \begin{pmatrix} -\mu_1^2 + \frac{1}{2}(\alpha_1 + \alpha_4)R^2 & 2\mu_2^2 - \frac{1}{2}\alpha_2 R^2 & -\frac{1}{\sqrt{2}}\mu_5 R & 0 \\ 2\mu_2^2 - \frac{1}{2}\alpha_2 R^2 & -\mu_1^2 + \frac{1}{2}(\alpha_1 + \alpha_3)R^2 & \frac{1}{\sqrt{2}}\mu_4 R & 0 \\ -\frac{1}{\sqrt{2}}\mu_5 R & \frac{1}{\sqrt{2}}\mu_4 R & -\mu_3^2 + \frac{1}{2}\rho_2 R^2 & 0 \\ 0 & 0 & 0 & -\mu_3^2 + \rho_1 R^2 \end{pmatrix}, \tag{B3}$$

and for the charged scalars, in the basis $\{\phi_1^\pm, \phi_2^\pm, \chi_L^\pm, \chi_R^\pm\}$ we get,

$$\mathcal{M}_{\text{charged}}^2 = \begin{pmatrix} -\mu_1^2 + \frac{1}{2}(\alpha_1 + \alpha_4)R^2 & 2\mu_2^2 - \frac{1}{2}\alpha_2 R^2 & -\frac{1}{\sqrt{2}}\mu_5 R & 0 \\ 2\mu_2^2 - \frac{1}{2}\alpha_2 R^2 & -\mu_1^2 + \frac{1}{2}(\alpha_1 + \alpha_3)R^2 & \frac{1}{\sqrt{2}}\mu_4 R & 0 \\ -\frac{1}{\sqrt{2}}\mu_5 R & \frac{1}{\sqrt{2}}\mu_4 R & -\mu_3^2 + \frac{1}{2}\rho_2 R^2 & 0 \\ 0 & 0 & 0 & -\mu_3^2 + \rho_1 R^2 \end{pmatrix}. \tag{B4}$$

The neutral gauge boson mass matrix, in the basis $\{Z_L^\mu, Z_R^\mu, B^\mu\}$, is,

$$\mathcal{M}_Z^2 = \begin{pmatrix} 0 & 0 & 0 \\ 0 & 0 & 0 \\ 0 & \frac{1}{4}g_R^2 R^2 & -\frac{1}{4}g_{BL}g_R R^2 \\ 0 & -\frac{1}{4}g_{BL}g_R R^2 & \frac{1}{4}g_{BL}^2 R^2 \end{pmatrix}. \tag{B5}$$

For the charged bosons, in the basis $\{W_L^{\mu\pm}, W_R^{\mu\pm}\}$,

$$\mathcal{M}_W^2 = \begin{pmatrix} 0 & 0 \\ 0 & \frac{1}{4}g_R^2 R^2 \end{pmatrix}. \tag{B6}$$

In addition to the field-dependent masses, we also need thermal self-energies of the fields for daisy resummation. These are obtained from the high-T expansion of the one-loop thermal potential. Substituting Eq. (3.9) in Eq. (3.7) gives, to leading order,

$$V_{1T}^{\text{high}} = \frac{T^2}{24}\left(\sum_b n_b m_b^2 + \frac{1}{2}\sum_f n_f m_f^2\right). \quad \text{(B7)}$$

Here, index b runs over bosons, while index f runs over fermions. Each sum can be expressed as the trace of the respective matrix. Thermal mass matrices are then expressed as, $\Pi_{ij} = c_{ij}T^2$, where c_{ij} are,

$$c_{ij} = \frac{1}{T^2}\frac{\partial^2}{\partial\varphi_i\partial\varphi_j}V_{1T}^{\text{high}}\bigg|_{\langle\cdots\rangle}. \quad \text{(B8)}$$

We define,

$$d_1 = \frac{1}{48}(9g_L^2 + 9g_R^2 + 8(2\alpha_1 + \alpha_3 + \alpha_4 + 5\lambda_1 + 2\lambda_3)), \quad \text{(B9)}$$

$$d_1' = d_1 + \frac{y_{33}^2}{4} + \frac{\tilde{y}_{33}^2}{4}, \quad \text{(B10)}$$

$$d_2 = \frac{1}{3}(2\alpha_2 + 3\lambda_4), \quad \text{(B11)}$$

$$d_2' = d_2 + \frac{y_{33}\tilde{y}_{33}}{4}, \quad \text{(B12)}$$

$$d_L = \frac{1}{48}(3g_{BL}^2 + 9g_L^2 + 8(2\alpha_1 + \alpha_3 + \alpha_4 + 3\rho_1 + \rho_2)), \quad \text{(B13)}$$

$$d_R = \frac{1}{48}(3g_{BL}^2 + 9g_R^2 + 8(2\alpha_1 + \alpha_3 + \alpha_4 + 3\rho_1 + \rho_2)). \quad \text{(B14)}$$

We obtain the following thermal mass matrices:

$$\Pi_{\text{CPE}} = T^2\begin{pmatrix} d_1' & d_2' & 0 & 0 \\ d_2' & d_1' & 0 & 0 \\ 0 & 0 & d_L & 0 \\ 0 & 0 & 0 & d_R \end{pmatrix}, \quad \text{(B15)}$$

$$\Pi_{\text{CP0}} = T^2\begin{pmatrix} d_1' & -d_2' & 0 & 0 \\ -d_2' & d_1' & 0 & 0 \\ 0 & 0 & d_L & 0 \\ 0 & 0 & 0 & d_R \end{pmatrix}, \quad \text{(B16)}$$

$$\Pi_{\text{charged}} = T^2\begin{pmatrix} d_1 & -d_2 & 0 & 0 \\ -d_2 & d_1 & 0 & 0 \\ 0 & 0 & d_L & 0 \\ 0 & 0 & 0 & d_R \end{pmatrix}. \quad \text{(B17)}$$

The thermal mass matrices for the longitudinal gauge bosons are,

$$\Pi_Z = \frac{T^2}{6}\begin{pmatrix} 13g_L^2 & 0 & 0 \\ 0 & 13g_R^2 & 0 \\ 0 & 0 & 6g_{BL}^2 \end{pmatrix}, \quad \text{(B18)}$$

$$\Pi_{W^\pm} = \frac{13}{6}T^2\begin{pmatrix} g_L^2 & 0 \\ 0 & g_R^2 \end{pmatrix}. \quad \text{(B19)}$$

The mass of each species with the above thermal corrections is obtained as the eigenvalue of the matrix, $m^2(R) + \Pi(T)$. After diagonalization, the longitudinal polarization of the photon becomes massive, while the transverse components remain massless.

APPENDIX C: NEUTRINO MASSES IN DLRSM

We have not taken into account a mechanism for generating neutrino mass in our version of DLRSM. In this section, we argue the minimal way of incorporating neutrino mass in this model do not give any additional contribution to the GW phenomenology of the model.

To demonstrate our point, we consider the model discussed in Refs. [12,13]. Small neutrino masses are generated radiatively by the Zee mechanism, by adding a charged singlet scalar $\delta^+ \sim (1,1,1,2)$ to DLRSM. In our notation, the Majorana Lagrangian is,

$$-\mathcal{L}_{LR}^M = \gamma_L L_L L_L \delta^+ + \gamma_R L_R L_R \delta^+ + \gamma_1 \chi_L^T i\sigma_2 \Phi \chi_R \delta^- + \gamma_1 \chi_L^T i\sigma_2 \tilde{\Phi}\chi_R \delta^- + \text{H.c.}, \quad \text{(C1)}$$

where, $\gamma_{L,R}, \gamma_1, \gamma_2$ are the new Yukawa couplings. As there is no tree-level right-handed neutrino mass, the contribution of the RH neutrinos to the effective potential is zero. However, the quartic terms involving δ^+ modify the mixing between the charged scalars. In the basis of $\{\phi_1^\pm, \phi_2^\pm, \chi_L^\pm, \chi_R^\pm, \delta^\pm\}$, the additional contribution to the charged mass matrix, $\mathcal{M}_{\text{charged}}^2$ is,

$$\delta\mathcal{M}^2_{\text{charged}} = v_R^2 \begin{pmatrix} 0 & 0 & 0 & 0 & \frac{\gamma_2}{2}\frac{v_L}{v_R} \\ 0 & 0 & 0 & 0 & -\frac{\gamma_1}{2}\frac{v_L}{v_R} \\ 0 & 0 & 0 & 0 & \frac{(\gamma_1\kappa_2+\gamma_2\kappa_1)}{2v_R} \\ 0 & 0 & 0 & 0 & -\frac{v_L(\gamma_1\kappa_1+\gamma_2\kappa_2)}{2v_R^2} \\ \frac{\gamma_2}{2}\frac{v_L}{v_R} & -\frac{\gamma_1}{2}\frac{v_L}{v_R} & \frac{(\gamma_1\kappa_2+\gamma_2\kappa_1)}{2v_R} & -\frac{v_L(\gamma_1\kappa_1+\gamma_2\kappa_2)}{2v_R^2} & 0 \end{pmatrix}. \tag{C2}$$

Each of the nonzero entries is suppressed by a factor v_L/v_R or $\kappa_{1,2}/v_R$ compared to v_R^2. Therefore the mixing of the charged scalars of DLRSM with δ^+ is negligible, while their mixing among themselves remains unchanged. In the field-dependent mass matrix, we put $v_L \to 0$, $\kappa_{1,2} \to 0$, and $v_R \to R$, by which the additional mixing matrix, $\delta\mathcal{M}^2_{\text{charged}}(R)$, vanishes entirely. Hence the presence of δ^+ does not alter the field-dependent mass matrices and therefore does not contribute to the effective potential.

---

[1] Jogesh C. Pati and Abdus Salam, Lepton number as the fourth color, Phys. Rev. D **10**, 275 (1974); **11**, 703(E) (1975).

[2] R. N. Mohapatra and Jogesh C. Pati, A natural left-right symmetry, Phys. Rev. D **11**, 2558 (1975).

[3] Rabindra N. Mohapatra and Jogesh C. Pati, Left-right gauge symmetry and an "isoconjugate" model of *CP* violation, Phys. Rev. D **11**, 566 (1975).

[4] G. Senjanovic and Rabindra N. Mohapatra, Exact left-right symmetry and spontaneous violation of parity, Phys. Rev. D **12**, 1502 (1975).

[5] Goran Senjanovic, Spontaneous breakdown of parity in a class of gauge theories, Nucl. Phys. **B153**, 334 (1979).

[6] Alessio Maiezza, Goran Senjanović, and Juan Carlos Vasquez, Higgs sector of the minimal left-right symmetric theory, Phys. Rev. D **95**, 095004 (2017).

[7] N. G. Deshpande, J. F. Gunion, B. Kayser, and Fredrick Olness, Left-right-symmetric electroweak models with triplet Higgs field, Phys. Rev. D **44**, 837 (1991).

[8] Goran Senjanovic, Is left–right symmetry the key?, Mod. Phys. Lett. A **32**, 1730004 (2017).

[9] J. Schechter and J. W. F. Valle, Neutrino decay and spontaneous violation of lepton number, Phys. Rev. D **25**, 774 (1982).

[10] Rabindra N. Mohapatra and Deepinder P. Sidhu, Gauge theories of weak interactions with left-right symmetry and the structure of neutral currents, Phys. Rev. D **16**, 2843 (1977).

[11] K. S. Babu and V. S. Mathur, Radiatively induced seesaw mechanism for neutrino masses, Phys. Rev. D **38**, 3550 (1988).

[12] Pavel Fileviez Perez, Clara Murgui, and Sebastian Ohmer, Simple left-right theory: Lepton number violation at the LHC, Phys. Rev. D **94**, 051701 (2016).

[13] Pavel Fileviez Perez and Clara Murgui, Lepton flavour violation in left-right theory, Phys. Rev. D **95**, 075010 (2017).

[14] K. S. Babu and Anil Thapa, Left-right symmetric model without Higgs triplets, arXiv:2012.13420.

[15] Ernest Ma, Dark-matter fermion from left-right symmetry, Phys. Rev. D **85**, 091701 (2012).

[16] Mariana Frank, Chayan Majumdar, P. Poulose, Supriya Senapati, and Urjit A. Yajnik, Exploring $0\nu\beta\beta$ and leptogenesis in the alternative left-right model, Phys. Rev. D **102**, 075020 (2020).

[17] Lukáš Gráf, Sudip Jana, Ajay Kaladharan, and Shaikh Saad, Gravitational wave imprints of left-right symmetric model with minimal Higgs sector, J. Cosmol. Astropart. Phys. 05 (2022) 003.

[18] Evgeny K. Akhmedov, Manfred Lindner, Erhard Schnapka, and J. W. F. Valle, Dynamical left-right symmetry breaking, Phys. Rev. D **53**, 2752 (1996).

[19] B. P. Abbott *et al.*, Observation of gravitational waves from a binary black hole merger, Phys. Rev. Lett. **116**, 061102 (2016).

[20] Pau Amaro-Seoane *et al.*, Laser interferometer space antenna, arXiv:1702.00786.

[21] Naoki Seto, Seiji Kawamura, and Takashi Nakamura, Possibility of direct measurement of the acceleration of the universe using 0.1-Hz band laser interferometer gravitational wave antenna in space, Phys. Rev. Lett. **87**, 221103 (2001).

[22] Vincent Corbin and Neil J. Cornish, Detecting the cosmic gravitational wave background with the big bang observer, Classical Quantum Gravity **23**, 2435 (2006).

[23] M. Punturo *et al.*, The Einstein telescope: A third-generation gravitational wave observatory, Classical Quantum Gravity **27**, 194002 (2010).

[24] Benjamin P. Abbott *et al.*, Exploring the sensitivity of next generation gravitational wave detectors, Classical Quantum Gravity **34**, 044001 (2017).

[25] Chiara Caprini *et al.*, Science with the space-based interferometer eLISA. II: Gravitational waves from cosmological phase transitions, J. Cosmol. Astropart. Phys. 04 (2016) 001.

[26] Peter Athron, Csaba Balázs, Andrew Fowlie, Lachlan Morris, and Lei Wu, Cosmological phase transitions: From perturbative particle physics to gravitational waves, Prog. Part. Nucl. Phys. **135**, 104094 (2024).

[27] Pierre Auclair *et al.*, Cosmology with the laser interferometer space antenna, Living Rev. Relativity **26**, 5 (2023).

[28] Chiara Caprini and Daniel G. Figueroa, Cosmological backgrounds of gravitational waves, Classical Quantum Gravity **35**, 163001 (2018).

[29] P. S. Bhupal Dev and A. Mazumdar, Probing the scale of new physics by Advanced LIGO/VIRGO, Phys. Rev. D **93**, 104001 (2016).

[30] Andrea Addazi, Antonino Marcianò, and Roman Pasechnik, Probing trans-electroweak first order phase transitions from gravitational waves, MDPI Phys. **1**, 92 (2019).

[31] Dhruv Ringe, Probing intermediate scale Froggatt-Nielsen models at future gravitational wave observatories, Phys. Rev. D **107**, 015030 (2023).

[32] Vedran Brdar, Lukas Graf, Alexander J. Helmboldt, and Xun-Jie Xu, Gravitational waves as a probe of left-right symmetry breaking, J. Cosmol. Astropart. Phys. 12 (2019) 027.

[33] Mingqiu Li, Qi-Shu Yan, Yongchao Zhang, and Zhijie Zhao, Prospects of gravitational waves in the minimal left-right symmetric model, J. High Energy Phys. 03 (2021) 267.

[34] Debasish Borah and Arnab Dasgupta, Probing left-right symmetry via gravitational waves from domain walls, Phys. Rev. D **106**, 035016 (2022).

[35] Véronique Bernard, Sébastien Descotes-Genon, and Luiz Vale Silva, Constraining the gauge and scalar sectors of the doublet left-right symmetric model, J. High Energy Phys. 09 (2020) 088.

[36] Siddhartha Karmakar, Jai More, Akhila Kumar Pradhan, and S. Uma Sankar, Constraints on the doublet left-right symmetric model from Higgs data, J. High Energy Phys. 03 (2023) 168.

[37] Joydeep Chakrabortty, Rinku Maji, and Stephen F. King, Unification, proton decay and topological defects in non-SUSY GUTs with thresholds, Phys. Rev. D **99**, 095008 (2019).

[38] Sasmita Mishra and Urjit A. Yajnik, Spontaneously broken parity and consistent cosmology with transitory domain walls, Phys. Rev. D **81**, 045010 (2010).

[39] Debasish Borah and Sasmita Mishra, Spontaneous R-parity breaking, left-right symmetry and consistent cosmology with transitory domain walls, Phys. Rev. D **84**, 055008 (2011).

[40] Piyali Banerjee and Urjit Yajnik, Domain walls and *CP* violation with left right supersymmetry: Implications for leptogenesis and electron EDM, J. High Energy Phys. 07 (2021) 039.

[41] Z. A. Borboruah and U. A. Yajnik, Left-right symmetry breaking and gravitational waves: A tale of two phase transitions, arXiv: 2212.05829.

[42] Yue Zhang, Haipeng An, Xiangdong Ji, and Rabindra N. Mohapatra, General *CP* violation in minimal left-right symmetric model and constraints on the right-handed scale, Nucl. Phys. **B802**, 247 (2008).

[43] P. S. Bhupal Dev, Rabindra N. Mohapatra, and Yongchao Zhang, Probing the Higgs sector of the minimal left-right symmetric model at future hadron colliders, J. High Energy Phys. 05 (2016) 174.

[44] Sergio Ferrando Solera, Antonio Pich, and Luiz Vale Silva, Direct bounds on left-right gauge boson masses at LHC Run 2, J. High Energy Phys. 02 (2024) 027.

[45] Serguei Chatrchyan *et al.*, Observation of a new boson at a mass of 125 GeV with the CMS experiment at the LHC, Phys. Lett. B **716**, 30 (2012).

[46] G. Aad *et al.* (ATLAS Collaboration), Combined measurements of Higgs boson production and decay using up to 80 fb^{-1} of proton-proton collision data at $\sqrt{s} = 13$ TeV collected with the ATLAS experiment, Phys. Rev. D **101**, 012002 (2020).

[47] The ATLAS collaboration, Constraints on the Higgs boson self-coupling from the combination of single-Higgs and double-Higgs production analyses performed with the ATLAS experiment, Report No. ATLAS-CONF-2019-049, 2019, https://cds.cern.ch/record/2693958?ln=en.

[48] Mariano Quiros, Finite temperature field theory and phase transitions, in *ICTP Summer School in High-Energy Physics and Cosmology, Trieste, Italy* (1999), pp. 187–259 [arXiv: hep-ph/9901312].

[49] Mikko Laine and Aleksi Vuorinen, *Basics of Thermal Field Theory* (Springer, New York, 2016), 10.1007/978-3-319-31933-9.

[50] Sidney R. Coleman and Erick J. Weinberg, Radiative corrections as the origin of spontaneous symmetry breaking, Phys. Rev. D **7**, 1888 (1973).

[51] L. Dolan and R. Jackiw, Symmetry behavior at finite temperature, Phys. Rev. D **9**, 3320 (1974).

[52] James M. Cline and Pierre-Anthony Lemieux, Electroweak phase transition in two Higgs doublet models, Phys. Rev. D **55**, 3873 (1997).

[53] M. E. Carrington, The effective potential at finite temperature in the Standard Model, Phys. Rev. D **45**, 2933 (1992).

[54] Rajesh R. Parwani, Resummation in a hot scalar field theory, Phys. Rev. D **45**, 4695 (1992); **48**, 5965(E) (1993).

[55] Peter Arnold and Olivier Espinosa, Effective potential and first-order phase transitions: Beyond leading order, Phys. Rev. D **47**, 3546 (1993).

[56] Steven Weinberg, Gauge and global symmetries at high temperature, Phys. Rev. D **9**, 3357 (1974).

[57] Can Kilic and Sivaramakrishnan Swaminathan, Can a Pseudo-Nambu-Goldstone Higgs lead to symmetry non-restoration?, J. High Energy Phys. 01 (2016) 002.

[58] Patrick Meade and Harikrishnan Ramani, Unrestored electroweak symmetry, Phys. Rev. Lett. **122**, 041802 (2019).

[59] Andrei D. Linde, Dynamical symmetry restoration and constraints on masses and coupling constants in gauge theories, JETP Lett. **23**, 64 (1976), http://jetpletters.ru/ps/1795/article_27429.shtml.

[60] Steven Weinberg, Mass of the Higgs boson, Phys. Rev. Lett. **36**, 294 (1976).

[61] Carroll L. Wainwright, CosmoTransitions: Computing cosmological phase transition temperatures and bubble profiles with multiple fields, Comput. Phys. Commun. **183**, 2006 (2012).

[62] M. Quiros, Field theory at finite temperature and phase transitions, Helv. Phys. Acta **67**, 451 (1994), https://inspirehep.net/literature/774592.

[63] Hiren H. Patel and Michael J. Ramsey-Musolf, Baryon washout, electroweak phase transition, and perturbation theory, J. High Energy Phys. 07 (2011) 029.

[64] Arindam Chatterjee, AseshKrishna Datta, and Subhojit Roy, Electroweak phase transition in the Z_3-invariant NMSSM: Implications of LHC and dark matter searches and prospects of detecting the gravitational waves, J. High Energy Phys. 06 (2022) 108.

[65] Andrei D. Linde, Fate of the false vacuum at finite temperature: Theory and applications, Phys. Lett. **100B**, 37 (1981).

[66] Wei-Chih Huang, Francesco Sannino, and Zhi-Wei Wang, Gravitational waves from Pati-Salam dynamics, Phys. Rev. D **102**, 095025 (2020).

[67] Jose R. Espinosa, Thomas Konstandin, Jose M. No, and Geraldine Servant, Energy budget of cosmological first-order phase transitions, J. Cosmol. Astropart. Phys. 06 (2010) 028.

[68] N. Aghanim *et al.*, Planck 2018 results. VI. Cosmological parameters, Astron. Astrophys. **641**, A6 2020; **652**, C4(E) (2021).

[69] Huai-Ke Guo, Kuver Sinha, Daniel Vagie, and Graham White, Phase transitions in an expanding universe: Stochastic gravitational waves in standard and non-standard histories, J. Cosmol. Astropart. Phys. 01 (2021) 001.

[70] Eric Thrane and Joseph D. Romano, Sensitivity curves for searches for gravitational-wave backgrounds, Phys. Rev. D **88**, 124032 (2013).

[71] Sachiko Kuroyanagi, Kazunori Nakayama, and Jun'ichi Yokoyama, Prospects of determination of reheating temperature after inflation by DECIGO, Prog. Theor. Exp. Phys. **2015**, 13E02 (2015).

[72] Kai Schmitz, New sensitivity curves for gravitational-wave experiments, J. High Energy Phys. 01 (2021) 097.

[73] J. de Blas *et al.*, Higgs boson studies at future particle colliders, J. High Energy Phys. 01 (2020) 139.

[74] Guy D. Moore and Tomislav Prokopec, Bubble wall velocity in a first order electroweak phase transition, Phys. Rev. Lett. **75**, 777 (1995).

[75] Guy D. Moore and Tomislav Prokopec, How fast can the wall move? A study of the electroweak phase transition dynamics, Phys. Rev. D **52**, 7182 (1995).

[76] Dietrich Bodeker and Guy D. Moore, Can electroweak bubble walls run away?, J. Cosmol. Astropart. Phys. 05 (2009) 009.